The Astrophysical Journal, 752:86 (25pp), 2012 June 20 doi:10.1088/0004-637X/752/2/86

RESOLVING THE GALAXIES WITHIN A GIANT Lyα NEBULA: WITNESSING THE FORMATION OF A GALAXY GROUP?

Moire K. M. Prescott[1,2,13], Arjun Dey[3], Mark Brodwin[4,5], Frederic H. Chaffee[6,14], Vandana Desai[7], Peter Eisenhardt[8], Emeric Le Floc'h[9], Buell T. Jannuzi[3], Nobunari Kashikawa[10], Yuichi Matsuda[11], and B. T. Soifer[7,12]

[1] Department of Physics, University of California, Santa Barbara, CA 93106, USA; mkpresco@physics.ucsb.edu
[2] Steward Observatory, University of Arizona, 933 North Cherry Avenue, Tucson, AZ 85721, USA
[3] National Optical Astronomy Observatory, 950 North Cherry Avenue, Tucson, AZ 85719, USA
[4] Harvard-Smithsonian Center for Astrophysics, 60 Garden Street, Cambridge, MA 02138, USA
[5] Department of Physics, University of Missouri-Kansas City, 5110 Rockhill Road, Kansas City, MO 64110, USA
[6] Department of Physics and Astronomy, University of North Carolina, Chapel Hill, NC 27599, USA
[7] Spitzer Science Center, California Institute of Technology, MS 220-6, Pasadena, CA 91125, USA
[8] Jet Propulsion Laboratory, California Institute of Technology, MC 169-327, 4800 Oak Grove Drive, Pasadena, CA 91109, USA
[9] Laboratoire AIM, CEA/DSM, CNRS, University of Paris, 91191 Gif-sur-Yvette, France
[10] Optical and Infrared Astronomy Division, National Astronomical Observatory of Japan, Mitaka, Tokyo 181-8588, Japan
[11] Department of Physics, Science Site, Durham University, South Road, Durham DH1 3LE, UK
[12] Caltech Optical Observatories, California Institute of Technology, Pasadena, CA 91125, USA
Received 2011 May 25; accepted 2012 April 11; published 2012 May 30

ABSTRACT

Detailed analysis of the substructure of Lyα nebulae can put important constraints on the physical mechanisms at work and the properties of galaxies forming within them. Using high-resolution *Hubble Space Telescope* (*HST*) imaging of a Lyα nebula at $z \approx 2.656$, we have taken a census of the compact galaxies in the vicinity, used optical/near-infrared colors to select system members, and put constraints on the morphology of the spatially extended emission. The system is characterized by (1) a population of compact, low-luminosity ($\sim 0.1\ L^*$) sources—17 primarily young, small ($R_e \approx 1$–2 kpc), disky galaxies including an obscured active galactic nucleus—that are all substantially offset ($\gtrsim$20 kpc) from the line-emitting nebula; (2) the lack of a central galaxy at or near the peak of the Lyα emission; and (3) several nearly coincident, spatially extended emission components—Lyα, He II, and UV continuum—that are extremely smooth. These morphological findings are difficult to reconcile with theoretical models that invoke outflows, cold flows, or resonant scattering, suggesting that while all of these physical phenomena may be occurring, they are not sufficient to explain the powering and large extent of Lyα nebulae. In addition, although the compact galaxies within the system are irrelevant as power sources, the region is significantly overdense relative to the field galaxy population (by at least a factor of four). These observations provide the first estimate of the luminosity function of galaxies within an individual Lyα nebula system and suggest that large Lyα nebulae may be the seeds of galaxy groups or low-mass clusters.

Key words: galaxies: evolution – galaxies: formation – galaxies: high-redshift

Online-only material: color figures

1. INTRODUCTION

Giant (∼100 kpc), radio-quiet Lyα nebulae (or Lyα "blobs") that have been discovered in the distant universe by virtue of their extremely luminous Lyα emission ($\sim 10^{44}$ erg s^{-1}) are thought to be regions of ongoing massive galaxy formation. When studied in detail, these systems show complex morphologies, obscured active galactic nuclei (AGNs), and/or associated star-forming galaxies (e.g., Francis et al. 1996; Ivison et al. 1998; Steidel et al. 2000; Palunas et al. 2004; Chapman et al. 2004; Matsuda et al. 2004, 2007; Basu-Zych & Scharf 2004; Dey et al. 2005; Geach et al. 2007; Smith et al. 2008; Prescott et al. 2009; Ouchi et al. 2009; Yang et al. 2011). There is strong evidence that the largest Lyα nebulae are rare (Saito et al. 2006; Yang et al. 2009, 2010; Prescott 2009; Matsuda et al. 2011) and typically reside in the most overdense regions of the universe (e.g., Palunas et al. 2004; Matsuda et al. 2004, 2005, 2009; Saito et al. 2006; Prescott et al. 2008; Yang et al. 2009).

Unlike Lyα halos observed around quasars and radio galaxies (e.g., McCarthy 1993 and references therein; Weidinger et al. 2005; Miley et al. 2006; Barrio et al. 2008; Smith et al. 2009), the dominant power source responsible for these radio-quiet Lyα nebulae has been difficult to determine. Studies have investigated whether Lyα nebulae could be powered by galactic superwind outflows (e.g., Taniguchi & Shioya 2000; Taniguchi et al. 2001; Mori et al. 2004), photoionization by obscured AGNs or star formation (e.g., Chapman et al. 2004; Basu-Zych & Scharf 2004; Geach et al. 2007, 2009; Prescott et al. 2009), or gravitational cooling within cold filaments ("cold flows"; e.g., Nilsson et al. 2006; Smith & Jarvis 2007; Dijkstra & Loeb 2009; Goerdt et al. 2010; Faucher-Giguère et al. 2010), but have come to a range of conclusions. It has also been suggested that the large extent of Lyα nebulae could be due to resonant scattering of Lyα photons from a central source, with recent work providing observational evidence for this effect around Lyman-break galaxies (Steidel et al. 2011). Thus, despite considerable study, the mechanisms responsible for the copious Lyα emission and the large extent of Lyα nebulae have remained controversial.

[13] TABASGO Postdoctoral Fellow.
[14] Currently at Gemini Observatory.

Table 1
HST Observations of LABd05

Instrument	Filter	Exposure Time (min)	λ_C	Bandpass Width	Rest-frame λ at $z \approx 2.656$
HST/ACS	*FR*462*N* ([O II] outer ramp)	216	4448 Å[a]	89 Å	Lyα λ1216
HST/ACS	*F*606*W* (broadband *V*)	129	5907 Å	2342 Å	1295–1936 Å
HST/ACS	*FR*601*N* ([O III] outer ramp)	129	5998 Å[a]	120 Å	He II λ1640
HST/NICMOS NIC2	*F*110*W* (broadband *J*)	281	1.1 μm	0.6 μm	2188–3829 Å
HST/NICMOS NIC2	*F*160*W* (broadband *H*)	281	1.6 μm	0.4 μm	3829–4923 Å

Note. [a] Ramp filters *FR*462*N* and *FR*601*N* were centered on Lyα and He II λ1640, respectively, at $z \approx 2.7$ during these observations.

The question of the substructure of Lyα nebulae has received much less attention, but it is a topic that can provide much-needed complementary clues to the origin of Lyα nebulae as well as to what they ultimately evolve into. As the potential physical mechanisms responsible for powering the Lyα emission each have morphological implications, studying the morphology of the spatially extended emission on kiloparsec and sub-kiloparsec scales can provide insight into the processes at work and the underlying powering mechanism in Lyα nebulae. In addition, taking a complete census of the diffuse and compact sources within Lyα nebulae and studying the relative positions and properties (luminosities, colors, morphologies, sizes) of the galaxies that reside within them is valuable for establishing the evolutionary state of these dynamic systems. Doing all of this, however, requires determining the membership of these crowded regions either with spectroscopy (typically feasible only for the brightest knots) or deep, high-resolution imaging that can resolve and put constraints on the spectral energy distribution (SED) of faint individual sources. As yet, very few radio-quiet Lyα nebulae have been imaged with the *Hubble Space Telescope* (*HST*), and those that have typically lack the critical high-resolution constraints above the Balmer break.

In this paper, we study the sub-kiloparsec structure of a giant Lyα nebulae at $z \approx 2.656$ using high-resolution imaging from *HST*. This Lyα nebula was discovered thanks to its extreme *Spitzer*/MIPS 24 μm emission and its extended morphology in broadband B_W imaging (LABd05; Dey et al. 2005, hereinafter Paper I). Roughly 20″ (∼160 kpc) in size with a Lyα luminosity of $\approx 1.7 \times 10^{44}$ erg s^{-1}, LABd05 rivals other known Lyα nebulae in energetics and complexity. The data presented in Paper I revealed at least three important components (and potential sources of ionization) in the system: (1) the strong 24 μm source, likely dominated by an obscured AGN, (2) a Lyman break galaxy (LBG) to the northeast of the nebula, and (3) a source that does not have a counterpart in the ground-based imaging but that was identified near the center of the Lyα emission due to the presence of narrow, spatially unresolved He II λ1640 and C IV λ1548,1550 emission lines in the ground-based spectrum. Follow-up narrowband imaging of the surrounding environment revealed that LABd05 resides within a very large filamentary structure at least 50 comoving Mpc in size (Prescott et al. 2008), and imaging polarization observations have demonstrated that the Lyα emission is not strongly polarized ($P < 9\%$, 3σ; Prescott et al. 2011), hinting that scattering may not be significant in this source.

While revealing, our previous studies were limited by ground-based resolution and depth, and our resulting knowledge of the system was incomplete. First, at ground-based resolution, it was unclear whether the system hosted other compact galaxies and whether the Lyα emission itself contained a compact central source or was clumpy on small scales. Second, it was unclear whether the 24 μm source and the LBG were important power sources for the Lyα nebula. The geometry of the system, with both the 24 μm source and the LBG offset from the centroid of the Lyα by 2.″5 ($\gtrsim$20 kpc in projection), argued against this possibility, and the observed SED of both sources suggested that, barring inhomogeneous obscuration, they were unlikely to power more than ∼20% of the Lyα emission. Finally, the source of the unresolved He II and C IV emission, which appeared to be centered within the Lyα emission, was uncertain. While He II and C IV emission often indicate shock excitation or a hard ionization source, no central galaxy (that could be driving shock-heating via a superwind) was visible in the ground-based imaging and, furthermore, the measured line ratios were inconsistent with shocks.

In the present work, we use high-resolution *HST*/Advanced Camera for Surveys (ACS) and NICMOS imaging to take a census of the compact sources within the system, measure their luminosities, morphologies, and locations relative to the line-emitting gas, investigate the question of the location and morphology of the He II-emitting region, and determine the morphology of the Lyα nebula itself. In Section 2, we describe our observations and reductions, and in Section 3 we present our results on the different components of the Lyα nebula system. Section 4 summarizes what we have learned about the small-scale morphology of LABd05 and explores the implications of these findings for our understanding of what causes the Lyα nebula phenomenon. We conclude in Section 5. In this paper, we assume the standard ΛCDM cosmology ($\Omega_M = 0.3$, $\Omega_\Lambda = 0.7$, $h = 0.7$); the angular scale at $z = 2.656$ is 7.96 kpc/″. All magnitudes are in the AB system (Oke 1974).

2. OBSERVATIONS AND REDUCTIONS

Paper I examined the properties of LABd05 using Keck/LRIS spectroscopy, optical imaging from the NOAO Deep Wide-Field Survey (NDWFS; Jannuzi & Dey 1999), and *Spitzer*/IRAC and MIPS imaging (Eisenhardt et al. 2004; Houck et al. 2005). The large-scale environment of LABd05 was studied using Subaru/Suprime-Cam intermediate-band *IA*445 Lyα imaging (Prescott et al. 2008), and constraints on the Lyα polarization of the system were obtained using imaging polarimetry with the Bok Telescope and the SPOL CCD Spectropolarimeter (Prescott et al. 2011). In this paper, we add high-resolution *HST*/ACS and NICMOS imaging to study the small-scale morphology and local environment of LABd05. Table 1 lists the instruments, filters, and total exposure times for the *HST* imaging. Figure 1 shows selected postage stamps from the multi-wavelength data set used in this work.

2.1. HST ACS Data

We obtained *HST* ACS imaging of LABd05 on UT 2006 January 13, 14, and 24 using the *F*606*W* (V_{606}) filter and two 2% ramp filters, *FR*462*N* (centered on Lyα at $z \approx 2.7$) and *FR*601*N*

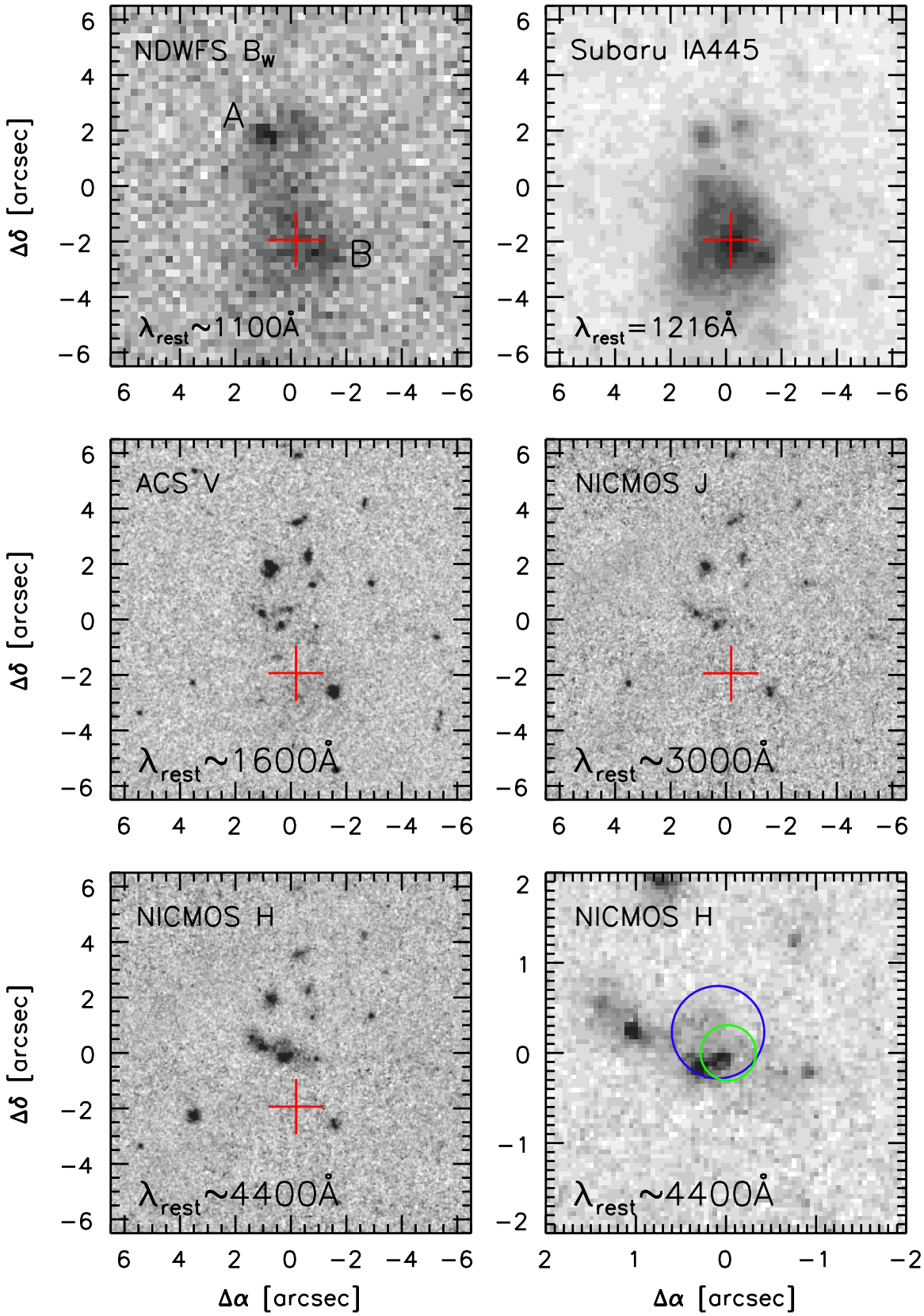

Figure 1. Multi-wavelength imaging of LABd05. In each panel, [0″,0″] is centered on the location of the obscured AGN (see Section 3.1.2), and the position of the Lyα centroid measured from the Subaru imaging is shown (red cross). The compact components identified in ground-based imaging (Galaxies "A" and "B" from Paper I) are labeled on the NDWFS B_W image. The lower right-hand panel shows a zoomed-in version of the NICMOS H_{160} image with the position of the MIPS 24 μm and IRAC 3.6 μm source positions indicated (blue and green 1σ error circles, respectively; Dey et al. 2005; Gorjian et al. 2008). At $z \approx 2.656$, 1″ corresponds to a physical scale of 7.96 kpc.

(A color version of this figure is available in the online journal.)

(centered on He II λ1640 at $z \approx 2.7$).[15] Basic image calibrations (overscan, bias, and dark subtraction, and flat fielding) were provided by the standard *HST* ACS pipeline with On-The-Fly-Reprocessing (OTFR) and the task *calacs*. We removed a residual offset in the bias level of the individual amplifiers on each of the ACS detectors (roughly a 2% effect relative to the background) by estimating the sky background in each amplifier separately using a sigma-clipped mean and subtracting it from the calibrated, flat-fielded individual exposures (the "_FLT" files). Using MultiDrizzle's default settings and no additional sky subtraction, we performed the distortion correction, cosmic-ray rejection, and image combination, yielding a final scale of 0.″05 pixel^{-1} and a field of view of 207″ × 205″. The point-spread-function (PSF) size for the ACS imaging is FWHM = 0.″07, as measured using the TinyTim PSF emulator.[16] The 5σ point-source limiting magnitudes for the ACS imaging are 28.3, 25.7, and 25.7 mag (0.″4 diameter aperture) for the $F606W$, $FR462N$, and $F601N$ filters, respectively.

The narrowband Lyα and He II imaging contain both line and continuum emission. To generate *HST* line-only Lyα and He II images, we scaled the V_{606} image by factors of 42.9 and 22.9, respectively (estimated empirically based on sources common to both images), and subtracted the result from the original narrowband images. The resulting *HST* line-only Lyα and He II images are discussed in Sections 3.2.1 and 3.2.2. To quantify the degree to which the He II and C IV emission lines in turn contaminate the V_{606} band, we measured the total V_{606} flux within the same spectroscopic aperture (4.″5 × 1.″5) used in Paper I to measure the He II and C IV fluxes, after convolving the V_{606} image to match the ground-based seeing (FWHM = 1″). Comparing the total V_{606} flux in the aperture ($1.15 \pm 0.01 \times 10^{-15}$ erg s^{-1} cm^{-2}) to the reported He II and C IV line fluxes ($4.07 \pm 0.04 \times 10^{-17}$ and $4.17 \pm 0.04 \times 10^{-17}$ erg s^{-1} cm^{-2}, respectively; Paper I), we find that the He II and C IV emission lines together contribute a small fraction of the V_{606}-band flux within this aperture ($\lesssim$7%), and therefore we do not apply a correction to the V_{606} image.

2.2. HST NICMOS Data

Using the NICMOS NIC2 camera on *HST*, we obtained high-resolution imaging of the source in the $F110W$ (J_{110}) and $F160W$ (H_{160}) filters—filters which at $z \approx 2.7$ bracket the Balmer/4000 Å break. The observations were taken during UT 2006 March 25 and 31, using a NIC-SPIRAL-DITH spiral dither pattern (three-point pattern with 0.″6375 point spacing).[17] The data were reduced primarily using NICRED (Magee et al. 2007). Once the data were calibrated and corrected for electronic ghosts, pedestal, cosmic-ray persistence, and count-rate nonlinearity, we made the final image mosaics using MultiDrizzle (Jedrzejewski et al. 2005) and a set of custom bad pixel masks. The final images were supersampled to match the ACS pixel scale (0.″05 pixel^{-1}) and have a field of view of 20″ × 20″. The PSF sizes are FWHM = 0.″09 and 0.″13, as measured using the TinyTim PSF emulator, and the 5σ point-source limiting magnitudes are 27.2 and 27.1 mag (0.″4 diameter aperture) for the J_{110} and H_{160} imaging, respectively.

2.3. Subaru Suprime-Cam Data

In this work, we make use of deep Subaru Lyα imaging that was obtained previously by Prescott et al. (2008) using the Subaru Telescope and the Suprime-Cam wide-field imager (Miyazaki et al. 2002). These observations used an intermediate-band filter $IA445$ ($\lambda_c \approx 4458$ Å, $\Delta\lambda_{\rm FWHM} \approx 201$ Å), centered on the Lyα line at the redshift of the nebula. The limiting magnitude of the Lyα image is 26.6 mag (5σ in a 2″ diameter aperture). Additional details on the observations and data reduction can be found in Prescott et al. (2008).

We generated a Subaru line-only Lyα image by subtracting off a smoothed version of the ACS V_{606}-band image. From the ground-based spectroscopy, we know that the source labeled "A" in the NDWFS B_W image (Figure 1) is an LBG at the redshift of the system and shows little if any Lyα emission or absorption (Paper I). A correct continuum subtraction should therefore leave the LBG with zero flux in the Subaru line-only Lyα image. We smoothed the V_{606} image to match the PSF of the Lyα image (FWHM = 0.″7), resampled to the same pixel scale as the Lyα image, measured the flux of the LBG in both the Lyα and V_{606}-band image (using a 1.″0 diameter aperture), scaled the V_{606} to match the flux of the LBG in the Lyα image, and subtracted the two to create a continuum-subtracted Lyα image. Since the V_{606} is a rather crude approximation to the continuum in the Lyα image, the accuracy of this continuum subtraction will vary with source color. We note that for all the galaxies at the redshift of the system, the subtraction should be relatively accurate; those that show residual emission in the Lyα image are likely Lyα emitters themselves. On the other hand, in the case of a known interloper galaxy at $z \approx 3.2$ (labeled "B" in Figure 1; Paper I), we expect our continuum subtraction procedure to overestimate the continuum (since at this redshift the $IA445$ band is sampling the continuum shortward of Lyα, which is typically depressed due to the Lyα forest). This is consistent with the slight evidence of oversubtraction that we see at the position of the interloper galaxy (Figure 2).

2.4. Image Registration

To ensure accurate image registration, we generated catalogs of source positions in each image using SExtractor (Bertin & Arnouts 1996) and registered all images to the NDWFS B_W frame using the IRAF tasks *ccmap* and *ccsetwcs*. We carried out the registration in three steps. First, the ACS V_{606} was convolved with a Gaussian kernel to match the PSF of the B_W image (FWHM = 0.″98). We registered the smoothed ACS V_{606} image to the NDWFS B_W image, applied the solution to the unsmoothed ACS V_{606} image, and then registered the ACS He II, NICMOS J_{110}, and NICMOS H_{160} images to the unsmoothed ACS V_{606} image. Finally, we registered the ACS Lyα image to the ACS He II image and the Subaru $IA445$ image to the NDWFS B_W image. This sequential procedure was used to maximize the number of common sources available to compute the astrometric solution for each image pair and to avoid compounding registration errors. Table 2 details the number of sources used in the registration and the final estimated astrometric uncertainty relative to the NDWFS B_W image. The NDWFS astrometry is tied to a frame defined by stars in the USNO-A2.0 catalog.

3. THE COMPONENTS OF THE NEBULA

Our multi-wavelength observations show that LABd05 contains a number of compact galaxies, diffuse rest-frame UV

[15] *HST* Cycle 14; GO 10591.
[16] TinyTim: http://www.stsci.edu/hst/observatory/focus/TinyTim.
[17] *HST* Cycle 14; GO 10591.

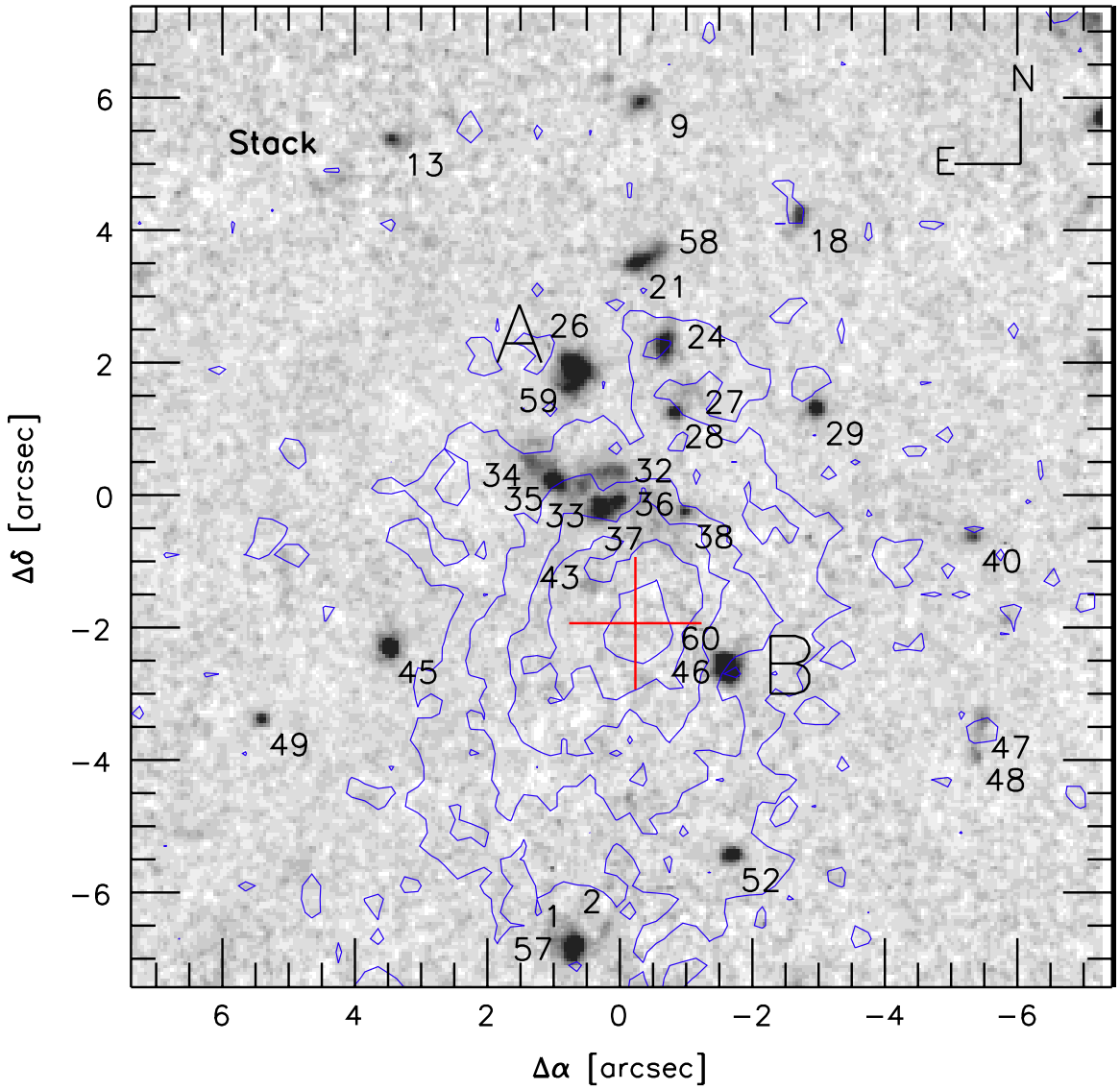

Figure 2. Composite image of LABd05 made by stacking the V_{606}, J_{110}, and H_{160} imaging. All compact sources detected above the 5σ limiting magnitude in the V_{606} band and located within 7″ of the obscured AGN (36, located at [0″,0″]) are labeled with the ID number used in Table 3. The contours correspond to Lyα surface brightness levels of $[1, 3, 5, 7, 9] \times 10^{-17}$ erg cm^{-2} s^{-1} arcsec^{-2}, as measured from the continuum-subtracted Subaru *IA*445 (Lyα) imaging. The position of the Lyα centroid measured from the Subaru imaging is shown (red cross).

(A color version of this figure is available in the online journal.)

Table 2
Astrometric Uncertainty[a]

Band	N_{obj}[b]	σ_α (arcsec)	σ_δ (arcsec)
NDWFS B_W	...	...	...
Subaru *IA*445	5062	0.10	0.09
ACS Lyα	8	0.17	0.13
ACS He II	18	0.12	0.10
ACS V_{606}	402	0.12	0.09
NICMOS J_{110}	6	0.12	0.09
NICMOS H_{160}	7	0.12	0.09

Notes.
[a] Astrometric uncertainty relative to the NDWFS B_W image.
[b] Number of common sources used to compute astrometric correction.

continuum emission, smooth Lyα emission, spatially extended He II emission, and an obscured AGN—all within a $\approx$10″ region. In this section, we explore each component of the Lyα nebula system in detail. In Section 4, we summarize the key morphological characteristics of this system and discuss the implications of these results for our understanding of the physical mechanisms at work in Lyα nebulae, their evolutionary state, and the properties of the galaxies forming within them.

3.1. Compact Sources

To determine the relative positions of all the sources in the vicinity of the Lyα nebula, we created a composite stack of the V_{606}, J_{110}, and H_{160} images, after convolving the V_{606}- and J_{110}-band images to the same PSF as the H_{160} image and dividing each image by the variance of the sky. We generated an initial list of source positions in the image stack using SExtractor (3σ threshold, minimum contiguous area of 4 pixels; Bertin & Arnouts 1996). All sources within 7″ that are detected above the 5σ limiting magnitude in the V_{606} band are labeled with ID numbers in Figure 2. We then generated an additional catalog of sources positions using the unconvolved V_{606}-band image and

Table 3
Properties of Compact Sources within LABd05

ID	Right Ascension (hr)	Declination (deg)	R_e[a] (arcsec)	n[a]	m_V[b] (AB)	$V_{606} - J_{110}$[b] (AB)	$J_{110} - H_{160}$[b] (AB)	System[c] Member?
36	14:34:10.981	33:17:32.48	0.39	19.9	28.24 ± 0.38	1.62 ± 0.43	1.69 ± 0.22	M1 (AGN)
26	14:34:11.036	33:17:34.47	0.17	1.0	25.36 ± 0.03	0.09 ± 0.07	0.32 ± 0.10	M1 (LBG)
59	14:34:11.041	33:17:34.14	0.27	1.4	26.15 ± 0.06	0.03 ± 0.15	0.36 ± 0.20	M1 (LBG)
28	14:34:10.913	33:17:33.80	0.15	2.0	26.86 ± 0.11	-0.34 ± 0.37	1.00 ± 0.42	M1
32	14:34:10.990	33:17:32.89	0.31	1.4	27.17 ± 0.15	0.20 ± 0.32	1.10 ± 0.33	M1
33	14:34:11.025	33:17:32.70	...	...	27.61 ± 0.21	0.95 ± 0.30	1.10 ± 0.25	M1
34	14:34:11.085	33:17:33.02	...	...	27.98 ± 0.30	1.35 ± 0.37	1.30 ± 0.24	M1
35	14:34:11.059	33:17:32.76	0.29	2.8	26.46 ± 0.08	0.72 ± 0.12	0.94 ± 0.12	M1
37	14:34:11.002	33:17:32.35	0.27	2.2	26.80 ± 0.11	1.10 ± 0.14	1.20 ± 0.11	M1
1	14:34:11.036	33:17:25.76	0.31	2.0	26.63 ± 0.09	0.96 ± 0.13	0.79 ± 0.11	M2
18	14:34:10.764	33:17:36.75	0.15	0.4	27.29 ± 0.16	0.67 ± 0.26	0.51 ± 0.30	M2
21	14:34:10.956	33:17:36.06	0.26	0.9	26.73 ± 0.10	0.68 ± 0.16	0.48 ± 0.18	M2
24	14:34:10.926	33:17:34.81	0.23	0.8	26.46 ± 0.08	0.34 ± 0.15	0.32 ± 0.21	M2
29	14:34:10.743	33:17:33.85	0.09	1.1	26.81 ± 0.11	0.31 ± 0.21	0.63 ± 0.25	M2
45	14:34:11.258	33:17:30.24	0.10	0.9	27.59 ± 0.21	1.71 ± 0.24	1.77 ± 0.11	M2
52	14:34:10.845	33:17:27.10	0.11	0.6	26.69 ± 0.10	0.24 ± 0.20	0.30 ± 0.29	M2
57	14:34:11.039	33:17:25.56	0.08	0.5	26.61 ± 0.09	0.94 ± 0.13	0.87 ± 0.11	M2
2	14:34:10.997	33:17:25.98	0.11	0.4	28.04 ± 0.32	...	...	...
27	14:34:10.897	33:17:34.12	0.21	0.2	27.97 ± 0.30	...	...	...
38	14:34:10.902	33:17:32.29	0.20	2.6	27.62 ± 0.22	...	...	...
43	14:34:11.015	33:17:31.17	0.16	0.2	27.54 ± 0.20	...	...	...
47	14:34:10.544	33:17:29.10	0.17	0.7	27.77 ± 0.25	...	...	...
48	14:34:10.551	33:17:28.61	0.16	0.8	27.76 ± 0.25	...	...	...
49	14:34:11.412	33:17:29.15	0.08	0.7	27.47 ± 0.19	...	...	...
9	14:34:10.955	33:17:38.49	0.17	0.9	27.19 ± 0.15	0.82 ± 0.22	0.01 ± 0.32	NM
13	14:34:11.251	33:17:37.90	0.09	0.9	27.18 ± 0.15	0.67 ± 0.24	-0.29 ± 0.45	NM
40	14:34:10.555	33:17:31.92	0.11	0.7	27.46 ± 0.19	0.79 ± 0.29	-0.42 ± 0.57	NM
58	14:34:10.936	33:17:36.24	0.50	4.1	27.53 ± 0.20	1.13 ± 0.26	0.05 ± 0.32	NM
46	14:34:10.850	33:17:29.85	0.11	0.9	25.49 ± 0.04	-0.10 ± 0.09	0.30 ± 0.13	NM ($z = 3.2$)[d]
60	14:34:10.854	33:17:30.05	0.13	1.0	25.97 ± 0.05	0.05 ± 0.12	0.24 ± 0.18	NM ($z = 3.2$)[d]

Notes.
[a] Morphological measurements R_e and n denote the effective radius and Sérsic index as measured by GALFIT (Section 3.1.4).
[b] Aperture magnitudes for the V_{606}, J_{110}, and H_{160} bands were computed using 0.″4 diameter apertures and aperture corrections of [1.15, 1.52, 1.76].
[c] Membership categories based on optical/NIR colors and proximity (see Section 3.1.3): "M1"—likely system member inside a radius of 2.″1 from the AGN (36); "M2"—likely system member but beyond a radius of 2.″1 from the AGN (36); "NM"—likely non-member. Objects with membership confirmed by a spectroscopic redshift are indicated with parenthetical remarks. Sources with no membership designation were not well detected in one or more bands.
[d] V_{606} aperture magnitude uncorrected for contamination by Lyα emission at $z \approx 3.2$ ($F_{\mathrm{Ly}\alpha} = 5.15 \times 10^{-17}$ erg s^{-1} cm^{-2}; Paper I).

the same parameters. This "V_{606}-only" catalog is necessary for our analysis of the number counts in the vicinity of LABd05 and the associated completeness corrections (Sections 3.1.1 and 4.2.1). In four cases (1, 21, 26, and 46) where SExtractor did not deblend an apparent close object pair, we manually added a second source position to the catalog (57, 58, 59, and 60, respectively), as described in Section 3.1.4. The current data are not sufficient to distinguish whether these objects are true companions or just morphological peculiarities (i.e., tidal features, dust lanes, etc.) associated with the primary object. We choose to treat these pairs as separate objects; however, combining them does not significantly change our conclusions. Individual postage stamps extracted from the image stack as well as the V_{606}-, J_{110}-, and H_{160}-band imaging are shown for all sources in the Appendix.

3.1.1. Optical and Near-infrared Photometry

We measured aperture photometry (0.″4 diameter apertures) in all three bands using the original unconvolved images and the positions derived from the image stack. The aperture size was chosen in order to contain as much flux as possible while minimizing contamination from neighboring sources. Aperture corrections of [1.15, 1.52, 1.76] were computed using the TinyTim PSF emulator and applied to the V_{606}, J_{110}, and H_{160} photometry, respectively. The resulting photometry is given in Table 3.

Without knowing the intrinsic colors of sources as a function of magnitude, it is difficult to estimate the completeness of the stacked catalog. Instead, we measured the completeness in the V_{606} band alone using the standard approach. First, we generated simulated galaxies, modeled as Gaussian profiles with $R_e = 0.''12$ (1 kpc, the typical size of non-member sources in the field; Section 3.1.4). We then inserted the simulated galaxies into the V_{606}-band imaging. We generated a "V_{606}-only" source catalog in the same manner as above and computed the completeness of our approach as a function of input V_{606} magnitude. The 80% and 50% completeness limits are 27.6 and 28.0 mag in the V_{606} band, respectively.

3.1.2. The Obscured AGN

Paper I postulated the existence of an obscured AGN at the position of the MIPS source based on the strong 24 μm emission

and the shape of the full SED. The corresponding detections in the IRAC bands agreed with the MIPS source position to within the astrometric uncertainty (≈0.″5) and showed that the source had a power-law SED in the mid-infrared, characteristic of an obscured AGN (e.g., Alonso-Herrero et al. 2006). Later *Spitzer*/Infrared Spectrograph (IRS) spectroscopy demonstrated that the infrared source is at the redshift of the Lyα nebula (Colbert et al. 2011), and millimeter and submillimeter observations have confirmed that the full SED is best approximated by an Mrk 231 (i.e., AGN-dominated) template (Bussmann et al. 2009; Yang et al. 2012). In Paper I, the physical location of the AGN within the system was uncertain due to the lower resolution of the IRAC and MIPS imaging, but the centroid of the mid-infrared emission appeared to be offset to the north of the brightest Lyα emission. The addition of the *HST*/NICMOS imaging revealed an extremely red source (36) located at the centroid of the IRAC and MIPS emission (Figure 1) that is very centrally concentrated (Section 3.1.4). This source shows a strong Balmer/4000 Å break—it is barely detected in V_{606} and J_{110} but very bright in H_{160}—and is one of the 17 sources flagged as members of the system (Section 3.1.3). It is located in a crowded region, with five close neighbors within ≈1.″5 (≈12 projected kpc), and diffuse emission visible in the NICMOS H_{160} band, suggestive of an ongoing merger. Since it is plausible to assume that the AGN lies near the deepest part of the gravitational potential well of this system, we will take the position of source 36 as the center of the system for our subsequent analysis. The measured projected offset between the AGN and the centroid of the Lyα emission (Section 3.2.1) is ≈1.″9 (≈15 kpc).

3.1.3. Assessing System Membership

Only two compact sources were previously identified from ground-based imaging (Paper I; see NDWFS B_W image in Figure 1). At the northeast corner of the system is a compact source—labeled "Galaxy A" in Paper I—that ground-based spectroscopic follow-up showed to be an LBG at the redshift of the system. The source at the southwest corner—named "Galaxy B" in Paper I—was argued to be an interloping system based on the identification of Lyα at $z \approx 3.2$ in the ground-based spectrum. The high-resolution *HST* imaging resolves both of these objects into two components: Galaxy A is associated with objects 26 and 59 and Galaxy B contains knots 46 and 60 (see Section 3.1.4 and the Appendix). Since the spectroscopic identification was done using ground-based spectroscopy that was unable to resolve the two components in each case, it is possible that these pairs are in fact due to chance coincidence. However, with separations of only ∼0.″2 (i.e., 1.6 kpc), chance projection is extremely unlikely, and the photometry shows that the colors of both components in each pair are similar. Given the ground-based spectroscopic redshift, the very small likelihood of a chance coincidence, and the similar colors, we will assume from here on that 26 and 59 are both associated with the Lyα nebula system at $z \approx 2.7$ and that 46 and 60 are both interlopers at $z \approx 3.2$.

To determine the membership of the remaining sources, we make use of the measured optical/NIR colors. Since the NICMOS J_{110} and H_{160} bands straddle the Balmer/4000 Å break at the redshift of the nebula, sources within the system should show red $J_{110} - H_{160}$ colors if they have evolved enough with time. While a full SED-fitting approach would be poorly constrained with only three bands, we can use this fact to identify other sources that are likely associated with the system.

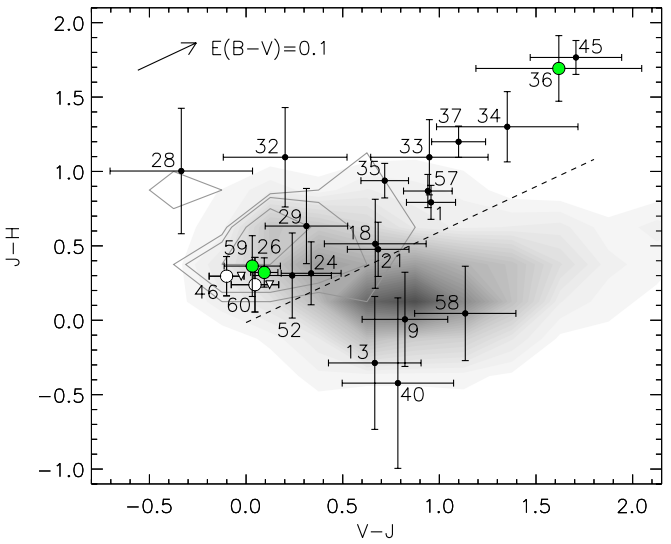

Figure 3. $J_{110} - H_{160}$ vs. $V_{606} - J_{110}$ color–color plot for compact sources in the vicinity of LABd05. Known spectroscopic members are denoted with large green circles (the LBG system, 26+59, and the counterpart to the obscured AGN, 36). The known spectroscopic interlopers (46+60) are shown as measured (large open circles) and after correcting for the contribution of Lyα emission to the V_{606} band (open triangles; see Table 3). The gray-scale contours represent all galaxies from the HUDF above the magnitude limits of our V_{606}, J_{110}, and H_{160} data; the line contours represent the subset with photometric redshifts at the redshift of LABd05 ($z_{\rm phot} = 2.656 \pm 0.15$; Coe et al. 2006). The dashed black line indicates the division used for membership assignment (Section 3.1.3). The appropriate reddening vector is shown for $E(B - V) = 0.1$ mag computed at $z \approx 2.656$.

(A color version of this figure is available in the online journal.)

We start by selecting the sample of sources that are within a radius of 7″ from the AGN (36) and that are brighter than the 5σ limiting magnitude in all three bands. In Figure 3, we plot the $V_{606} - J_{110}$ versus $J_{110} - H_{160}$ colors of the resulting sample along with gray-scale contours representing the expected color distribution of galaxies drawn from the field (taken from the Hubble Ultra Deep Field, HUDF, which used the same instrument and filters as this work; Coe et al. 2006). The subset of HUDF galaxies with photometric redshifts consistent with the systemic redshift to within typical photometric redshift errors ($z_{\rm photo} = 2.656 \pm 0.15$) is shown with line contours. While a handful of sources have colors entirely consistent with being drawn from the field (i.e., they are near the peak of the HUDF gray scale), there is also a locus of objects that is broadly consistent with being at the systemic redshift (i.e., they are within the line contours) but that extends along a line roughly parallel to the reddening vector toward much redder colors. These red colors are quite unusual for typical field galaxies, a hint that this locus may be composed primarily of system members with varying amounts of dust.

In Figure 4, we plot the same sample alongside a series of age tracks for simple stellar population models (single unreddened bursts, solar metallicity) at $z = 1.5$–4.0 as well as a constant star-forming model (solar metallicity) and a low-metallicity model ($Z = 0.0001$), both at the systemic redshift (Bruzual & Charlot 2003). We again see that the locus discussed above consists of sources that are consistent with the systemic redshift if we allow for a low to moderate amount of dust extinction ($E(B - V) \approx 0.0$–0.4 mag). We draw a dividing line in color–color space with a slope parallel to the reddening vector in order to select sources that are consistent with the systemic redshift, given typical photometric errors. Those to

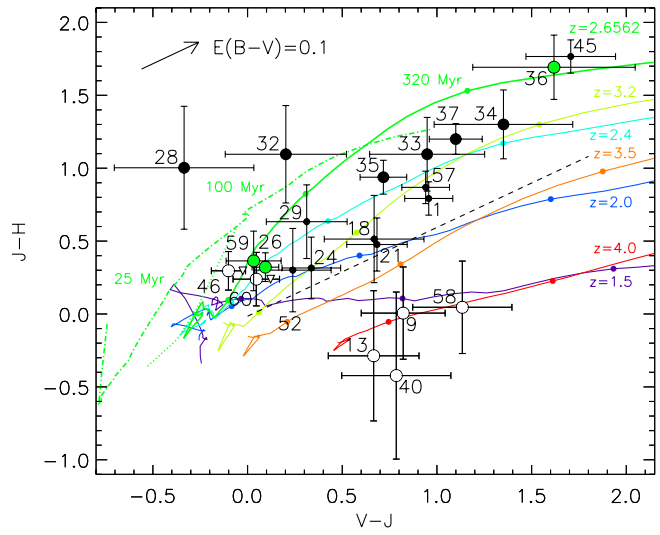

Figure 4. $J_{110} - H_{160}$ vs. $V_{606} - J_{110}$ color–color plot for compact sources in the vicinity of LABd05. Member sources in category "M1" are shown as large filled circles—with known spectroscopic members in green, i.e., the LBG system (26+59) and the obscured AGN (36)—and those in "M2" as small filled circles. Non-member sources ("NM") are shown as open circles; the known spectroscopic interlopers (46+60) are shown as measured (large open circles) and after correcting for the contribution of Lyα emission to the V_{606} band (open triangles; see Table 3). A series of single stellar population model age tracks (unreddened burst, solar metallicity, spanning burst ages of 5–1400 Myr; Bruzual & Charlot 2003) are overplotted for different redshifts. The thick green line corresponds to $z \approx 2.656$, the redshift of LABd05. The 25 Myr, 100 Myr, and 320 Myr positions along the tracks are indicated with small filled circles. For comparison, a constant star-forming model (dotted green line) and a low-metallicity model ($Z = 0.0001$, dot-dashed green line) are shown, both spanning the same age range at the redshift of LABd05. The dashed black line indicates the division used for membership assignment (Section 3.1.3). The appropriate reddening vector is shown for $E(B - V) = 0.1$ mag computed at $z \approx 2.656$.

(A color version of this figure is available in the online journal.)

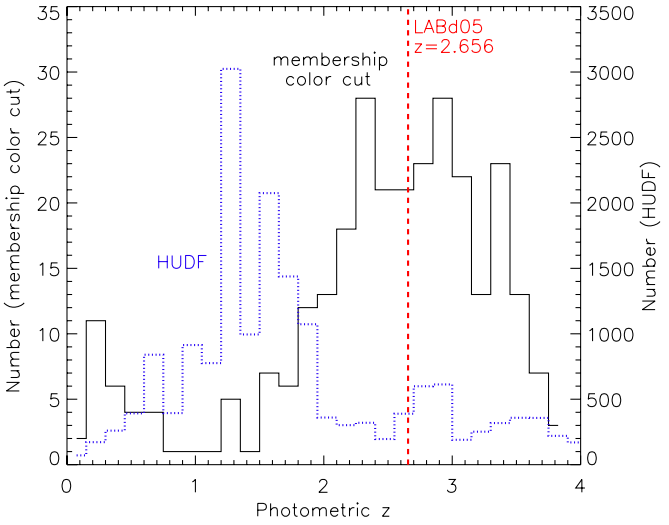

Figure 5. Photometric redshift distribution for galaxies in the HUDF that satisfy the color cut used for membership assignment in this work (black solid histogram) in comparison with the distribution for the full HUDF galaxy sample (blue dotted histogram; Coe et al. 2006). This comparison demonstrates that the proposed color cut is successful at selecting high-redshift sources (90% at $z > 1$) with the peak of the resulting redshift distribution centered on the redshift of LABd05 (red dashed line).

(A color version of this figure is available in the online journal.)

the upper left of the line we consider "members" and those to the lower right, "non-members" (designated "NM"). As a check on the effectiveness of our approach, we apply the same color cut to the HUDF galaxy catalog and plot a histogram of the photometric redshifts for this sub-sample (Figure 5). The color cut is effective at selecting high-redshift galaxies (90% are at $z_{\rm photo} \gtrsim 1$), and in contrast to the redshift distribution for the full HUDF sample, the photometric redshifts of HUDF galaxies selected using this simple color cut are peaked at the systemic redshift of LABd05 ($z_{\rm photo} \approx 2.66$). On the other hand, our color cut is clearly approximate. The comparison sample selected from the HUDF contains a small subset (10%) of galaxies with $z_{\rm photo} \lesssim 1$, which is consistent with the fact that for young (≈25 Myr) single burst models the predicted colors at $z \lesssim 1$ overlap those for higher redshifts. The color cut is also not able to reject the known interloper system at $z \approx 3.2$ (46 and 60, or Galaxy B). From Figure 5, this is not at all surprising, as the peak of the $z_{\rm photo}$ distribution is broad, spanning $2.1 \lesssim z_{\rm photo} \lesssim 3.2$. Furthermore, the fact that the interloper system is located at the young end of the age tracks in color–color space (Figure 4) is consistent with the detection of Lyα emission (Paper I).

We assess the robustness of our membership assignment further in Section 4.2.2. At this point, we subdivide the member sample based on the projected distance from the AGN (36). The nine sources within the radius of 2.″1 (chosen to include all spectroscopically confirmed members, 26, 59, and 36) are considered to be members with high confidence and designated "M1." The eight members outside this radius are designated "M2." In Figure 6, we see that all the member sources (circled) are offset by 1.″9–6.″7 (15–53 projected kpc) from the peak of the Lyα emission (Section 3.2.1), i.e., they effectively reside at the outskirts of the Lyα nebula.

3.1.4. Sizes and Morphologies

Our next step was to use GALFIT (Peng et al. 2002) to derive sizes and morphologies for the sources within the vicinity of LABd05. Visual inspection of the V_{606} image revealed that in addition to the many compact galaxies in the region, there is diffuse, spatially extended emission. In order to avoid biasing the fits for the compact sources, we began by subtracting off an approximate fit to this diffuse emission using GALFIT. We then fitted all remaining compact sources within 7″ of the AGN that have a peak surface brightness brighter than 25.3 mag arcsec^{-2} and an isophotal magnitude brighter than 29.0 AB mag in the V_{606} band. To speed up the process of fitting so many sources simultaneously, we performed the fits in small batches initially, i.e., fitting one to seven nearby sources at a time while masking the remaining sources. After experimentation showed that sources 1, 21, 26, and 46 were not being fitted well using single components, sources 57, 58, 59, and 60, respectively, were manually added to the catalog (as mentioned in Section 3.1). During the initial batch fitting, the positions of sources 57, 58, and 59 were then masked, while 60 was fitted normally. Once appropriate fitting parameters had been determined for all sources, we performed a final run of GALFIT on the original image, fixing all parameters for the compact sources to the pre-derived values. We allowed the few remaining special cases (57, 58, and 59) as well as the diffuse continuum component to be fitted freely by GALFIT. The entire fitting process was repeated using the fitting parameters derived for the diffuse continuum component in this final step as the initial guess for the first step. The resultant composite fit and corresponding residual images are shown in Figure 7. The centroids and morphological results for the compact sources derived from the V_{606} band are given in Table 3 and for the diffuse component in Table 4. We

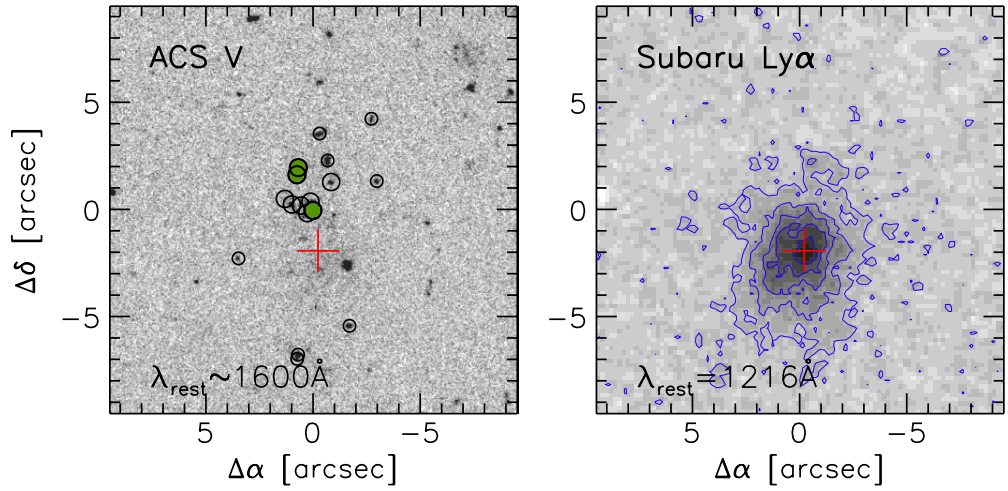

Figure 6. LABd05 galaxy membership. The obscured AGN is centered at [0″,0″] in both panels, and the position of the Lyα centroid measured from the Subaru imaging is shown as a red cross. Left: the ACS V_{606} image, with circles representing sources that have been flagged as members of the system based on optical/NIR colors and distance from the AGN ("M1" spectroscopic members: filled green circles, "M1": large black circles, "M2": small black circles; see Section 3.1.3). Right: the continuum-subtracted Subaru *IA*445 (Lyα) imaging, with contours at Lyα surface brightness levels of $[1, 3, 5, 7, 9] \times 10^{-17}$ erg cm^{-2} s^{-1} arcsec^{-2}. Note that the Lyα emission is offset by $\gtrsim$1.″9 $\approx$ 15 projected kpc from all of the member galaxies.

(A color version of this figure is available in the online journal.)

discuss this diffuse UV continuum component in further detail in Section 3.2.3.

3.2. Diffuse Components

In addition to the population of compact sources, LABd05 hosts several nearly coincident diffuse emission components.

3.2.1. Diffuse Lyα Emission

If the Lyα nebula is powered by sources within the nebula itself, then we would expect that to be reflected in the morphology of the Lyα emission. We used the high-resolution ACS Lyα imaging to look for spatially resolved knots or clumps that could signal the locations of the ionizing sources for the nebula. However, we find that the morphology of the Lyα nebula is smooth, with no significant substructure (Figure 8). At the depth of these observations, we would have detected point-source regions down to a Lyα flux of $F_{\mathrm{Ly}\alpha} = 2.6 \times 10^{-17}$ erg s^{-1} cm^{-2} (5σ in 0.″4 diameter apertures) or a Lyα luminosity of $L_{\mathrm{Ly}\alpha} = 1.5 \times 10^{42}$ erg s^{-1}. This corresponds to a star formation rate of $\approx$1.3 $M_{\odot}$ yr^{-1} (assuming Case B, $L_{\mathrm{Ly}\alpha} = 8.7 \times L_{\mathrm{H}\alpha}$; Kennicutt 1998). We can also rule out high surface brightness clumps within the cloud down to a peak surface brightness limit of $\approx$4.0 $\times 10^{-16}$ erg s^{-1} cm^{-2} arcsec^{-2} (3σ).

Deeper Lyα imaging at ground-based resolution obtained with the Subaru Telescope showed that the Lyα emission on larger scales has a smooth elliptical morphology that is well fitted by an exponential disk profile. Using GALFIT, we derived a centroid, effective radius, Sérsic index, position angle, and axis ratio for the Lyα emission (Table 4). The resulting surface brightness profile of the Lyα emission is shown in Figures 9 and 10. Surface brightness profiles were also computed for both the Subaru Lyα imaging and the ACS Lyα imaging using the IRAF task *ellipse*, where the ellipse parameters were constrained to the centroid, single position angle, and axis ratio of the GALFIT parametric fit to the Subaru Lyα imaging. In addition, we measured aperture photometry at the center of the nebula using a small aperture (1.″6 diameter) chosen to minimize contamination from neighboring compact sources (Table 4).

3.2.2. Diffuse He II Emission

From ground-based spectroscopy, LABd05 is known to have strong He II and C IV emission (Paper I) located near the center of the Lyα emission ([−0.″9,−2.″5]; Figure 11). The goal of our He II imaging was to better localize the He II-emitting region within the system, and given the depth of our observations, we would have detected the He II emission at an S/N $\approx$ 10 if it were emitted as a point source. However, the ACS He II imaging showed no detection down to a 5σ point-source limiting flux of 1.9×10^{-17} erg s^{-1} cm^{-2} (0.″4 diameter aperture) and a 3σ surface brightness limit of 3.3×10^{-16} erg s^{-1} cm^{-2} arcsec^{-2} (Figure 11). While we cannot, therefore, pinpoint the location of the He II emission beyond what was determined in Paper I, this non-detection does put a constraint on the size of the He II-emitting region. To quantify this, we inserted a series of simulated He II sources, modeled as Gaussian profiles scaled to match the measured He II flux and a range of FWHM sizes of 0.1–1.″0, into the He II image (Figure 11). For each of 100 Monte Carlo trials, we measured the observed flux of the simulated source ($F_{\mathrm{simulated}}$) as a function of FWHM and determined the FWHM for which the simulated source is detected at $F_{\mathrm{simulated}}/\sigma_{\mathrm{sky}} = 3$, where σ_{sky} is the 1σ limiting flux of the He II image (0.″4 diameter aperture). We conclude that the source of He II must be extended, with an FWHM $>$ 0.″58 in order to be undetected in our He II imaging. At the same time, the fact that the previous long-slit spectroscopy did not resolve the He II line puts an upper limit of $\sim$1″ on its true spatial extent (Paper I). This size range corresponds to a He II-emitting region that spans $\sim$4.6–8.0 kpc at the redshift of the nebula. These constraints are summarized in Table 4.

3.2.3. Diffuse Continuum Emission

The broadband ACS V_{606} data revealed diffuse emission located near the center of the Lyα nebula (Figure 7; Section 3.1.4). As He II and C IV emission at the systemic redshift are located within the V_{606} bandpass, and as the band also straddles Lyα at the redshift of Galaxy B (the interloper system at $z \approx 3.2$), we must first address the question of whether this diffuse V_{606}-band emission could be dominated by line emission. However, as we

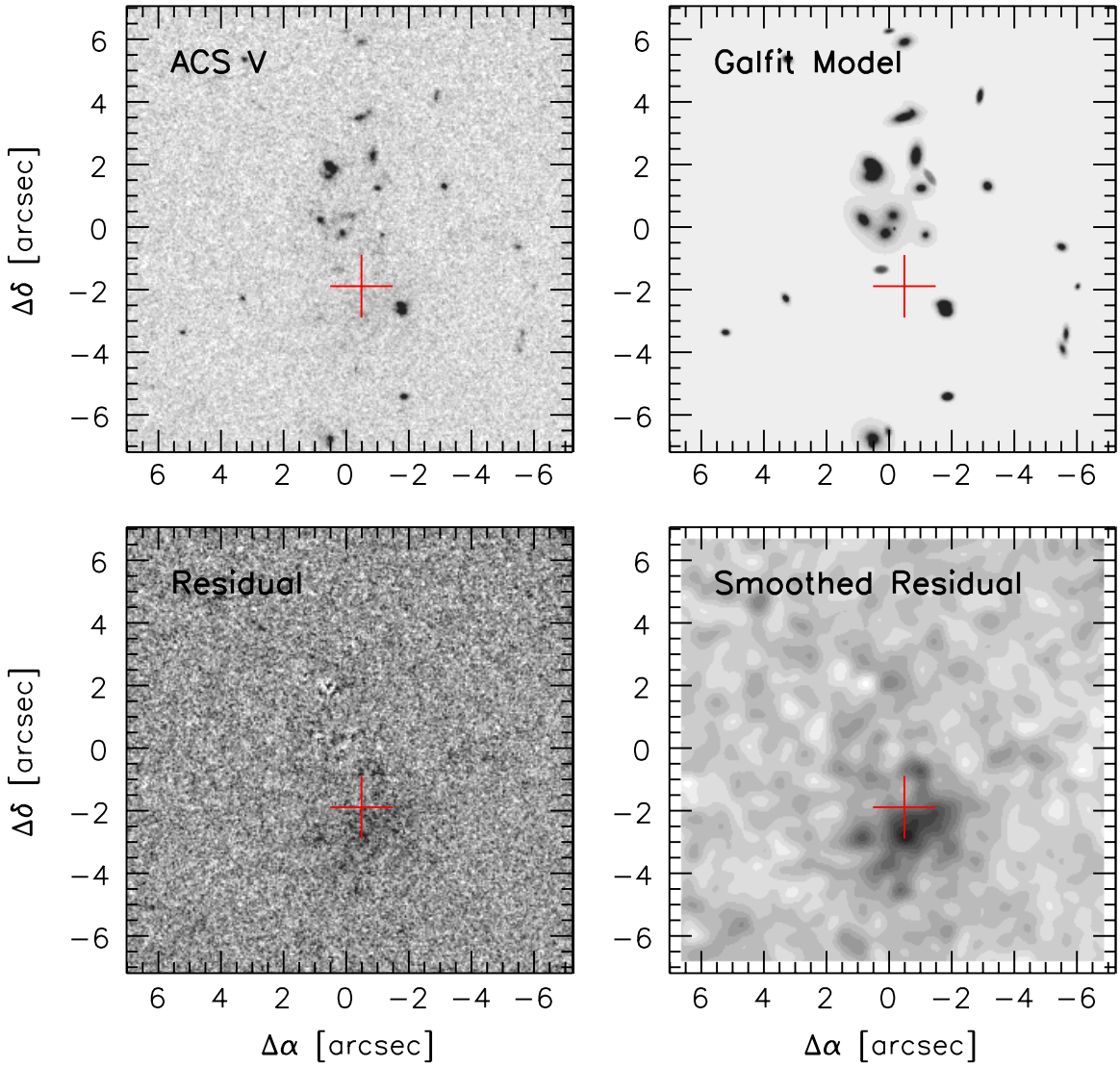

Figure 7. GALFIT parametric fit to the V_{606} imaging of LABd05. Top: the original V_{606} image and GALFIT model. Bottom: the residual image and smoothed residual image (FWHM = 10 pix = 0.″5 Gaussian kernel) reveal a diffuse UV continuum component. Note that the diffuse V_{606} continuum emission is nearly coincident with the Lyα centroid (red cross; an offset of ≈0.″8), and that both components are in turn offset by ≈1.″9–2.″6 ≈ 15–21 projected kpc from the position of the obscured AGN at [0″,0″].

(A color version of this figure is available in the online journal.)

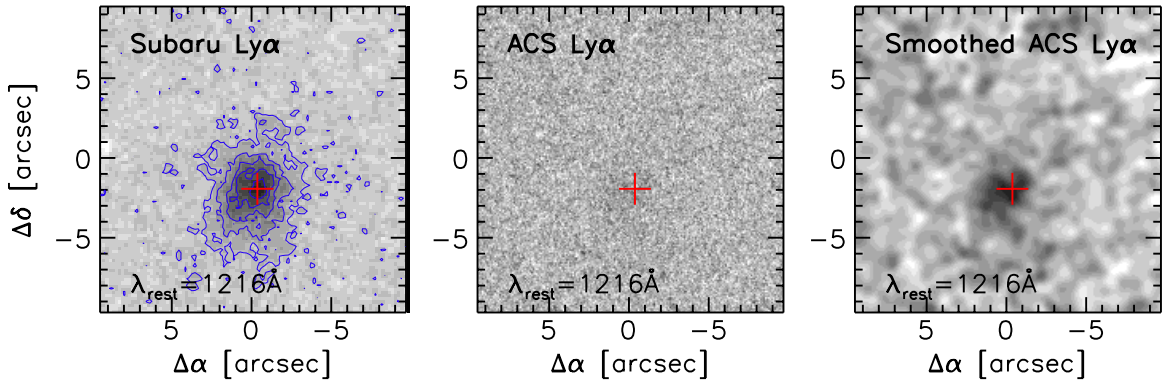

Figure 8. Lyα imaging of LABd05. The obscured AGN is centered at [0″,0″] in all panels, and the position of the Lyα centroid measured from the Subaru imaging is shown as a red cross. Left: the continuum-subtracted Subaru *IA*445 (Lyα) imaging, with contours at Lyα surface brightness levels of [1, 3, 5, 7, 9]$\times 10^{-17}$ erg cm^{-2} s^{-1} arcsec^{-2}. Middle: the ACS continuum-subtracted Lyα image. Right: the ACS continuum-subtracted Lyα image smoothed to match the PSF of the ground-based Subaru imaging (FWHM = 0.″7). No compact knots or clumps are detected in the ACS Lyα imaging.

(A color version of this figure is available in the online journal.)

Table 4
Properties of Diffuse Components within LABd05

		Diffuse Continuum		Diffuse Lyα	Diffuse He II
Band	V_{606}	J_{110}	H_{160}	$IA445$	
Rest-frame Wavelength (Å)	1298–1939 Å	2298–3720 Å	3829–4923 Å	1640–1716 Å	
GALFIT Parameters[a]					
Right ascension (hr)	14:34:10.940			14:34:10.986	14:34:10.925[b]
Declination (deg)	+33:17:29.87			+33:17:30.43	+33:17:29.92[b]
Size (arcsec)	$R_e = 1.67 \pm 0.08$			$R_e = 2.48 \pm 0.03$	FWHM = 0.58 − 1.0[c]
Sérsic index (n)	0.77 ± 0.05			0.73 ± 0.01	
Axis ratio (b/a)	0.77 ± 0.03			0.79 ± 0.01	
Position angle (°)	-43.49 ± 5.48			-15.51 ± 1.24	
Total magnitude (AB)	23.81 ± 0.04			21.99 ± 0.01	
Total luminosity					
(10^{28} erg s^{-1} Hz^{-1})	$L_\nu = 17.13 \pm 0.63$				
(10^{42} erg s^{-1})				$L_{\mathrm{Ly}\alpha} = 101.61 \pm 0.94$	
Aperture Photometry[d]					
Magnitude (AB)	25.39 ± 0.09	>25.75	>25.79	24.60 ± 0.01	
Luminosity					
(10^{28} erg s^{-1} Hz^{-1})	$L_\nu = 4.00 \pm 0.35$	$L_\nu < 2.87$	$L_\nu < 2.77$		
(10^{42} erg s^{-1})				$L_{\mathrm{Ly}\alpha} = 9.15 \pm 0.11$	$L_{\mathrm{He\,II}} = 2.35 \pm 0.02$[e]

Notes.
[a] Errors on morphological parameters are formal fitting errors reported by GALFIT but do not include errors resulting from the continuum subtraction or previous fitting of embedded compact sources. They therefore likely underestimate the true uncertainty in fitting this complex system.
[b] Approximate position of the He II source measured from ground-based spectroscopic data (Paper I).
[c] Limits on the size derived from ACS He II imaging and ground-based spectroscopic data, as described in Section 3.2.2.
[d] Aperture photometry measured at the center of the nebula within a small 1.″6 diameter aperture, chosen to avoid nearby compact sources. No aperture corrections were applied. Limits are 3σ values.
[e] He II luminosity measured within a 4.″5 × 1.″5 spectroscopic slit assuming $z = 2.6562$ (Paper I).

showed in Section 2.1, the He II and C IV emission lines together can contribute at most 7% of the V_{606}-band flux. The Lyα emission from Galaxy B ($F_{\mathrm{Ly}\alpha} = 5.15 \times 10^{-17}$ erg s^{-1} cm^{-2}; Paper I) can contribute at most another 4% of the V_{606}-band flux, but even this negligible fraction is likely a gross overestimate. The spectroscopic data show that the Lyα emission from Galaxy B is compact, centered on the interloper system, rather than spatially extended (Paper I). We conclude, therefore, that the diffuse V_{606}-band emission seen in LABd05 is indeed rest-frame UV continuum emission.

As described in Section 3.1.4, we measured the centroid, size, and luminosity of this component using GALFIT, avoiding contamination from nearby compact sources during the fitting process by constraining all the fitting parameters for the compact sources to the previously derived values. Table 4 gives the position, magnitude, effective radius, Sérsic index, position angle, and axis ratio of the diffuse component. The diffuse continuum component is well fitted by an exponential disk profile and the centroid is nearly coincident with that of the Lyα emission (offset by ≈0.″8). We measured aperture photometry at the center of the nebula in all three bands using a small aperture (1.″6 diameter) chosen to minimize contamination from neighboring compact sources (Table 4). The surface brightness profile of the diffuse continuum emission was also computed using the IRAF task *ellipse*, where the ellipse parameters were constrained to the centroid, single position angle, and axis ratio of the GALFIT parametric fit (Figures 9 and 10).

At the depth of these observations, we would have detected point-source regions with fluxes of 3.5×10^{-17} erg s^{-1} cm^{-2} (5σ, 0.″4 diameter aperture), corresponding to a stellar mass limit of $\approx 3.1 \times 10^7\ M_\odot$, assuming a 25 Myr simple stellar population (Bruzual & Charlot 2003). We can also rule out high surface brightness clumps down to a peak surface brightness limit of $\approx 9.5 \times 10^{-16}$ erg s^{-1} cm^{-2} arcsec^{-2} (3σ). However, it is worth remembering that if there are many lower mass sources distributed over this area, they would appear as unresolved diffuse continuum emission.

4. DISCUSSION

4.1. The Substructure of LABd05

The high-resolution imaging of *HST* provides a precise look at the sub-kiloparsec morphology of LABd05, with important implications for our understanding of the substructure of Lyα nebulae and the properties of the galaxies forming within them, as well as for determining what power sources are ultimately responsible for the Lyα emission. The key morphological characteristics of this Lyα nebula system are the following.

1. *Many compact, low-luminosity galaxies.* The system hosts 17 primarily small, disky, low-luminosity galaxies including an obscured AGN.
2. *Offset morphology.* All the compact sources within the system are located $\gtrsim$20 kpc away from the peak and centroid of the Lyα nebula.
3. *No central galaxy.* LABd05 has no central galaxy or compact source brighter than $\approx 0.03\ L^*$ visible within the highest surface brightness region of the Lyα nebula.
4. *Diffuse line and continuum emission.* While the compact sources appear to avoid the region of the nebula, there are three nearly spatially coincident extended emission components located near the center of the nebula: Lyα, He II, and rest-frame UV continuum emission.
5. *Smooth, non-filamentary morphology.* Both the Lyα emission and the diffuse UV continuum emission are smooth and show surface brightness profiles that are consistent with

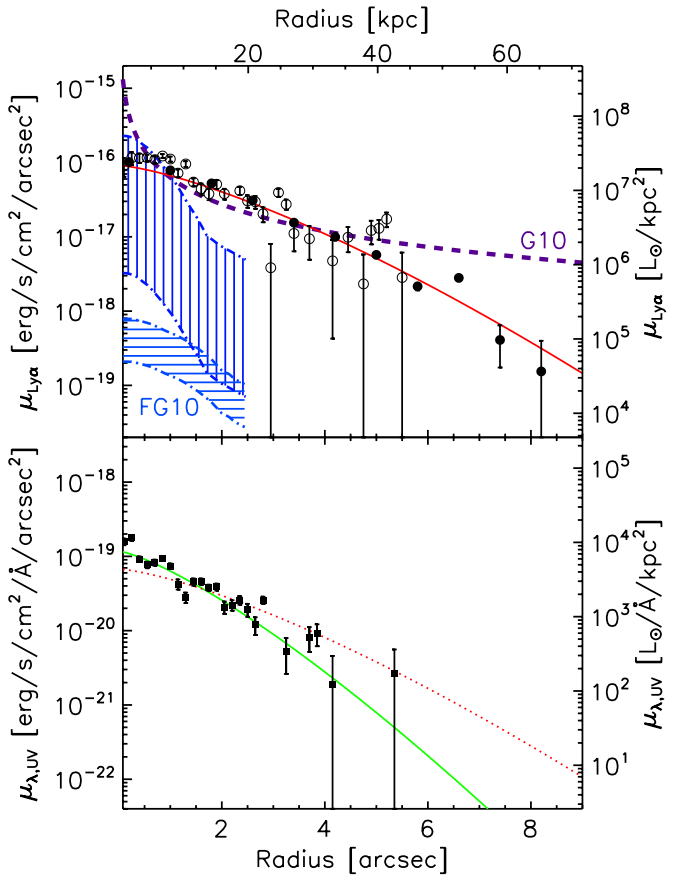

Figure 9. Surface brightness profiles of the Lyα and diffuse UV continuum emission in LABd05. Top: Lyα surface brightness profiles computed using the Subaru Lyα (filled circles) and ACS Lyα (small open circles) imaging as well as the GALFIT parametric fit to the Subaru Lyα imaging (red line). Predictions from cold flow simulations are overplotted and labeled with "G10" (dashed purple line; the prediction from Goerdt et al. 2010, scaled to match the total Lyα luminosity of LABd05 within a 5″ radius) and "FG10" (hatched blue regions bounded by dot-dashed lines; Faucher-Giguère et al. 2010), as discussed in Section 4.5. The observed profile of LABd05 is not well described by the predictions from existing cold flow simulations. Bottom: V_{606} surface brightness profile of the diffuse UV continuum emission in LABd05 (squares) as well as the GALFIT parametric fit (green line). A GALFIT parametric fit to the Subaru Lyα imaging from the top panel is reproduced for reference (dotted red line), after being scaled to match the total observed flux of the diffuse UV continuum within a radius of 3″. The centroids of the Lyα and diffuse UV continuum emission are offset by ≈0.″8.

(A color version of this figure is available in the online journal.)

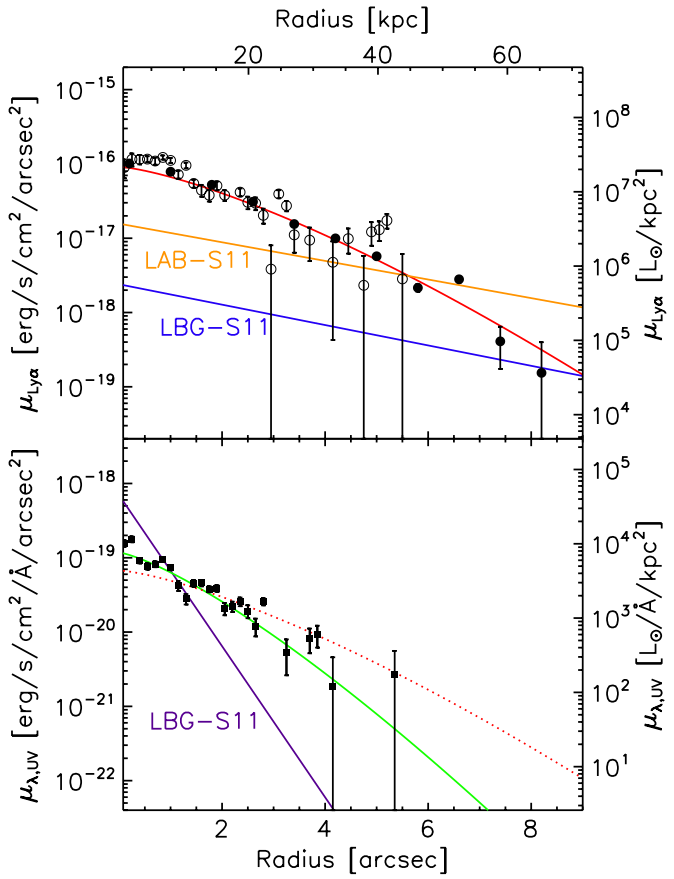

Figure 10. Surface brightness profiles of the Lyα and diffuse UV continuum emission in LABd05, as shown in Figure 9. Top: the stacked Lyα surface brightness profiles of continuum-selected galaxies ("LBG-S11"; blue line) and of Lyα nebulae ("LAB-S11"; orange line) from Steidel et al. (2011) are overplotted. Bottom: the stacked continuum surface brightness profile of continuum-selected galaxies from Steidel et al. (2011) is overplotted ("LBG-S11"; purple line). The stacked LBGs show compact UV emission surrounded by an extended Lyα halo, likely evidence for resonant scattering of Lyα photons generated in the core; in contrast the Lyα and UV surface brightness profiles for LABd05, while not identical, are strikingly similar in shape and extent.

(A color version of this figure is available in the online journal.)

exponential disks ($n \sim 0.7$–0.8) with moderate axis ratios ($b/a \sim 0.7$–0.8), i.e., they are not particularly clumpy or filamentary.

6. *Similar UV and Lyα surface brightness profiles.* The Lyα and UV continuum surface brightness profiles, while not identical, are comparable in shape and extent.

In what follows, we discuss each of the key morphological findings in detail. Focusing first on the compact sources, we show that the LABd05 system is overdense relative to the field, hosting a population of small, disky, low-luminosity galaxies that, while numerous, are irrelevant to the ionization of the nebula (Section 4.2). We then compare the remaining observed morphological characteristics to the expectations for Lyα nebulae driven by superwind outflow, cold flow, and resonant scattering scenarios and find significant discrepancies (Sections 4.3–4.6). We end with a discussion of the possibility that the LABd05 system is a forming galaxy group (Section 4.7).

4.2. Many Compact, Low-luminosity Galaxies

4.2.1. An Overdense Region

Even without determining the membership of individual nearby galaxies, it is clear from the high-resolution ACS and NICMOS imaging that there are a large number of compact sources in the vicinity of LABd05, more than would be expected for a region of this size in the field. Figure 12 shows the V_{606}-band number counts for sources detected above the 5σ limiting magnitude and located within a 7″ radius of the AGN in LABd05. For comparison, we show number count measurements drawn from our entire 207″ × 205″ ACS pointing as well as field measurements taken from the Hubble Deep Field-North and -South (HDF-N, HDF-S; Williams et al. 1996; Casertano et al. 2000), the HUDF (Beckwith et al. 2006; Coe et al. 2006), and the GOODS-North and -South fields (Giavalisco et al. 2004). Dividing the LABd05 number counts by those from the HUDF shows that the Lyα nebula system is overdense by at least a factor of 4 ± 1 relative to the field at magnitudes of $V_{606} < 27.5$ (Figure 13), with the uncertainty computed assuming Poisson statistics. If we further restrict the region of interest to a

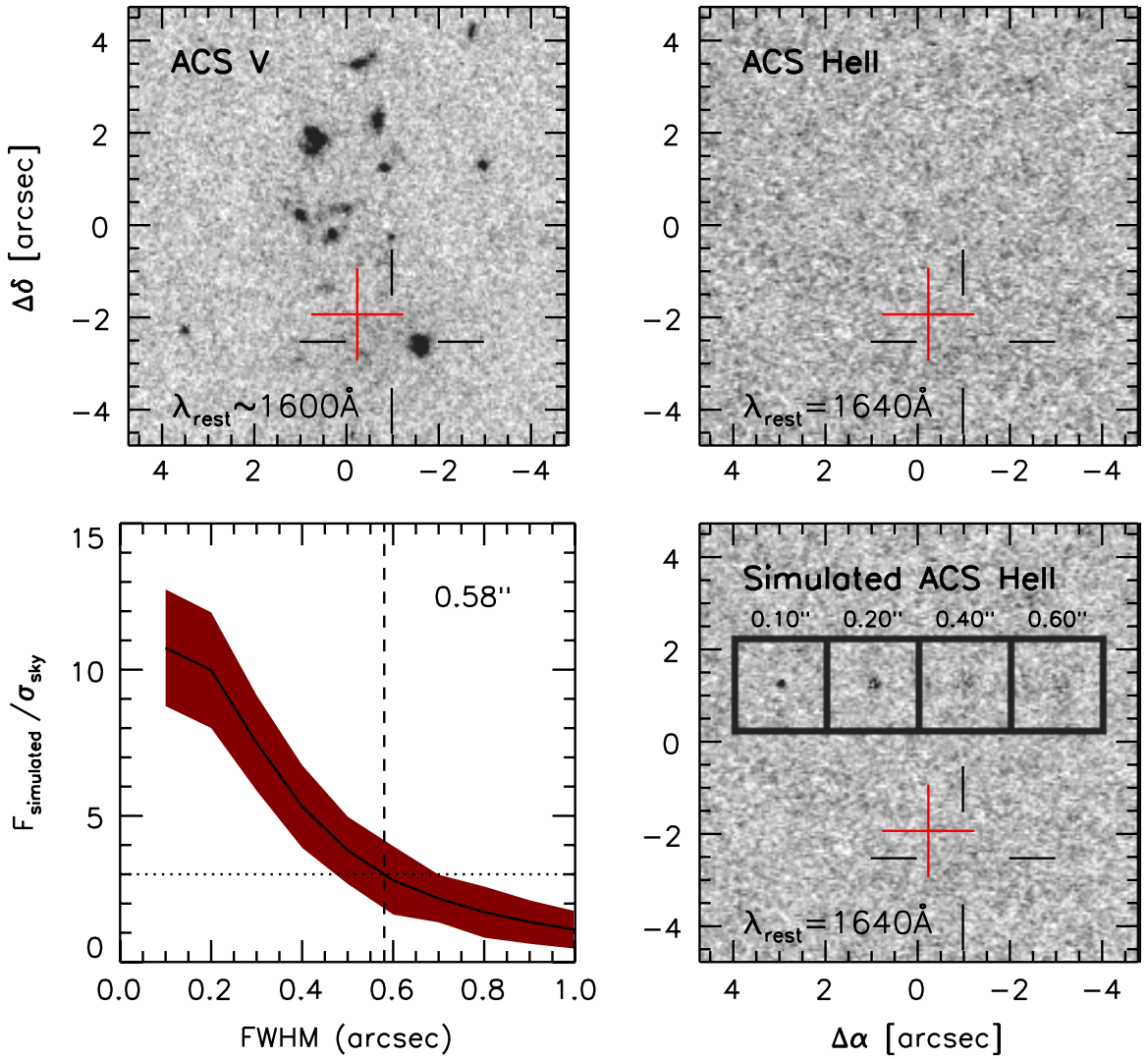

Figure 11. Limits on the size of the He II-emitting region derived from the continuum-subtracted ACS He II imaging. In all image panels, the position of the Lyα centroid measured from the Subaru imaging is shown (red cross), and the approximate position of the He II emission, as measured from ground-based spectroscopy, is indicated with black open cross hairs at [−0.″9,−2.″5]. Top: ACS V_{606} and continuum-subtracted He II imaging. Bottom left: ratio of the recovered flux of simulated He II sources with varying sizes ($F_{\rm simulated}$) divided by the 1σ limiting flux of the image ($\sigma_{\rm sky}$), shown as a function of the FWHM of the simulated source (0.″4 diameter apertures). The red band denotes the full range of results from 100 Monte Carlo trials. $F_{\rm simulated}/\sigma_{\rm sky} = 3$ is shown (dotted line) along with the derived lower limit on the size of the He II-emitting region (FWHM $> 0.''58$; dashed line). Any source smaller than this would have been detected at $>3\sigma$ (Section 3.2.2). Bottom right: a simulated He II image containing a representative set of model sources (FWHM = [0.″1, 0.″2, 0.″4, 0.″6]).

(A color version of this figure is available in the online journal.)

2.″5 radius region encompassing just the group of objects lying immediately to the north of the nebula (i.e., centered at [0″,+1.″5] in Figure 2), then the overdensity is a factor of 15 ± 5 above the field. We can derive a better estimate of the true overdensity factor relative to the field at this redshift by applying the membership color cut discussed in Section 3.1.3 to both the LABd05 and HUDF galaxy catalogs. In this case, the overdensity factor of the 7″ radius region approaches 12 ± 3 at magnitudes of $V_{606} < 27.5$. These high overdensity factors are not surprising if LABd05 is indeed a region of active galaxy formation destined to become a galaxy group or cluster.

4.2.2. Properties of the Member Galaxies

The previous section looked at the question of whether this region is overdense in a statistical sense relative to the field, i.e., without drawing on any knowledge of system membership. In Figure 14, we again show the V_{606} number counts (top panel), but in addition, we make use of our membership assignment to plot the number counts for sources that are likely within the system (bottom panel), i.e., the observed luminosity function. We find that the observed luminosity function of the M1+M2 subset is largely consistent with what we would predict statistically by taking the observed V_{606} number counts for the LABd05 region and simply subtracting off the expected V_{606} number counts for the field, as derived from the HUDF (Figure 14, dashed line). This good agreement between the statistical treatment of the previous section and the individual object membership treatment gives us confidence both that our membership assignment based on optical/NIR colors is reasonable and that our estimate of the observed luminosity function of the system is relatively robust, even if our membership assignment is not perfect on an object-by-object basis. To our knowledge, this is the first time

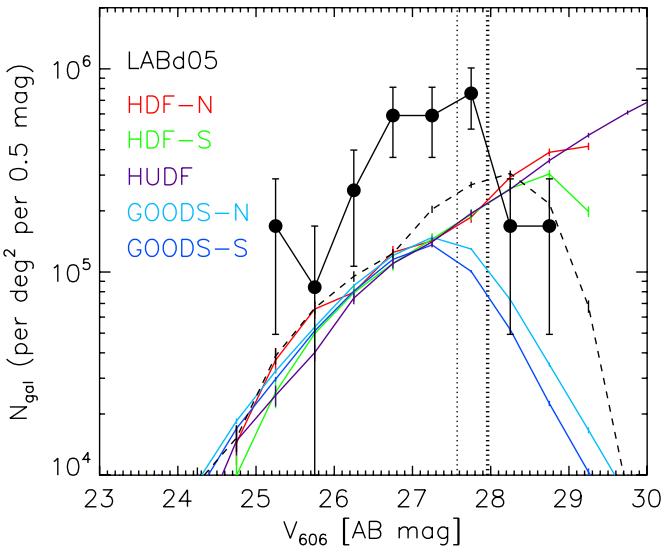

Figure 12. Number counts for sources detected above the 5σ limiting magnitude in the V_{606} band that are located within a $7''$ radius of the AGN in LABd05 (black solid line) and over the entire $207'' \times 205''$ ACS pointing (dashed black line). The 80% and 50% completeness limits are indicated (thin and thick dotted lines, respectively). The V_{606}-band number counts from the HDF-N and HDF-S (red and green lines; Williams et al. 1996; Casertano et al. 2000), the HUDF (purple line; Beckwith et al. 2006; Coe et al. 2006), and the GOODS-N and GOODS-S fields (light and dark blue lines; Giavalisco et al. 2004) are shown, remeasured using aperture magnitudes consistent with our analysis.

(A color version of this figure is available in the online journal.)

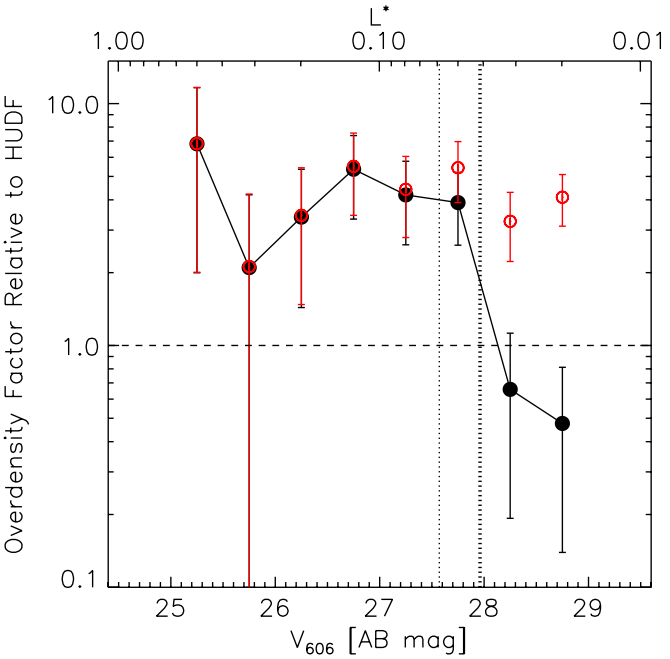

Figure 13. Overdensity scale factor, relative to the field number counts from HUDF, of galaxies within a $7''$ radius of the AGN that are detected above the 5σ limiting magnitude in the V_{606} band (black solid line). The LABd05 region is overdense by at least a factor of $\approx$4 relative to the field. The 80% and 50% completeness limits (thin and thick dotted lines, respectively) and the result of applying the completeness correction are shown (red open circles). The top axis is labeled in terms of L^* at $z \approx 3$ ($M^* = -20.8$; Reddy et al. 2008).

(A color version of this figure is available in the online journal.)

a luminosity function has been estimated for an individual Lyα nebula system, and it implies that LABd05 is dominated by low-luminosity galaxies. Assuming that M^* at $z \approx 2.7$ is ≈ -20.8 (AB mag at rest-frame 1700 Å; Reddy et al. 2008), which

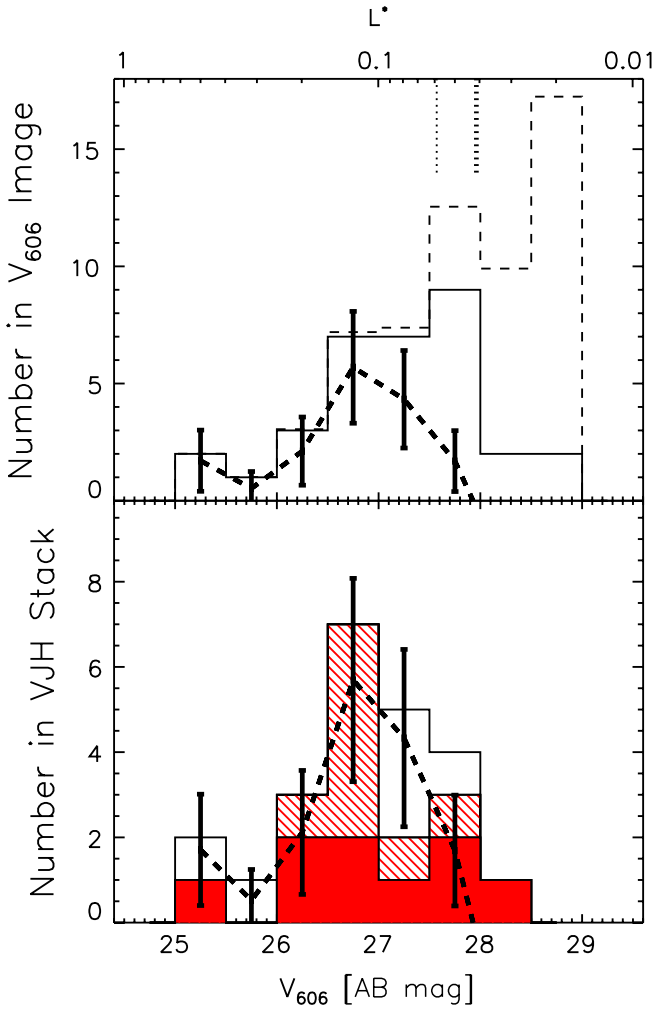

Figure 14. Luminosity function of galaxies within LABd05. Top: sources detected above the 5σ limiting magnitude in the V_{606} band and located within a $7''$ radius of the AGN (black open histogram) and corrected for incompleteness (thin dashed histogram). The 80% and 50% completeness limits are shown (thin and thick vertical dotted lines, respectively). Bottom: sources detected above the 5σ limiting magnitude *in all three bands* and located within a $7''$ radius of the AGN (black open histogram). The filled and hatched histograms represent galaxies in groupings "M1" and "M2," respectively (Section 3.1.3). The thick dashed curve in both panels is a "statistical" luminosity function for LABd05, as described in Section 4.2.2. The top axis is labeled in terms of L^* at $z \approx 3$ ($M^* = -20.8$; Reddy et al. 2008).

(A color version of this figure is available in the online journal.)

corresponds to $m^* \approx 24.49$ AB in apparent V_{606} magnitudes,[18] we find that the LABd05 system is dominated by $\approx 0.1\,L^*$ galaxies. Only one galaxy, the LBG (26), is more luminous than $\approx 0.4\,L^*$.

These data also reveal clues about the ages and morphologies of the galaxies within LABd05. The colors of sources within the system appear to be consistent with young ages ($\approx$25–100 Myr) and a range of dust extinctions ($E(B-V) \approx 0.0$–0.4 mag). The distribution of sizes and Sérsic indices of the galaxies in the vicinity of LABd05 are shown in Figure 15, with those that are likely associated with LABd05 shown as filled (subset M1) and hatched (subset M2) histograms. In general, the galaxies in the vicinity of LABd05 are small ($R_e = 0.5$–3 kpc), with Sérsic

[18] The central wavelength of V_{606} is $\lambda_c \approx 5907$ Å observed ≈ 1600 Å in the rest frame at $z \approx 2.7$.

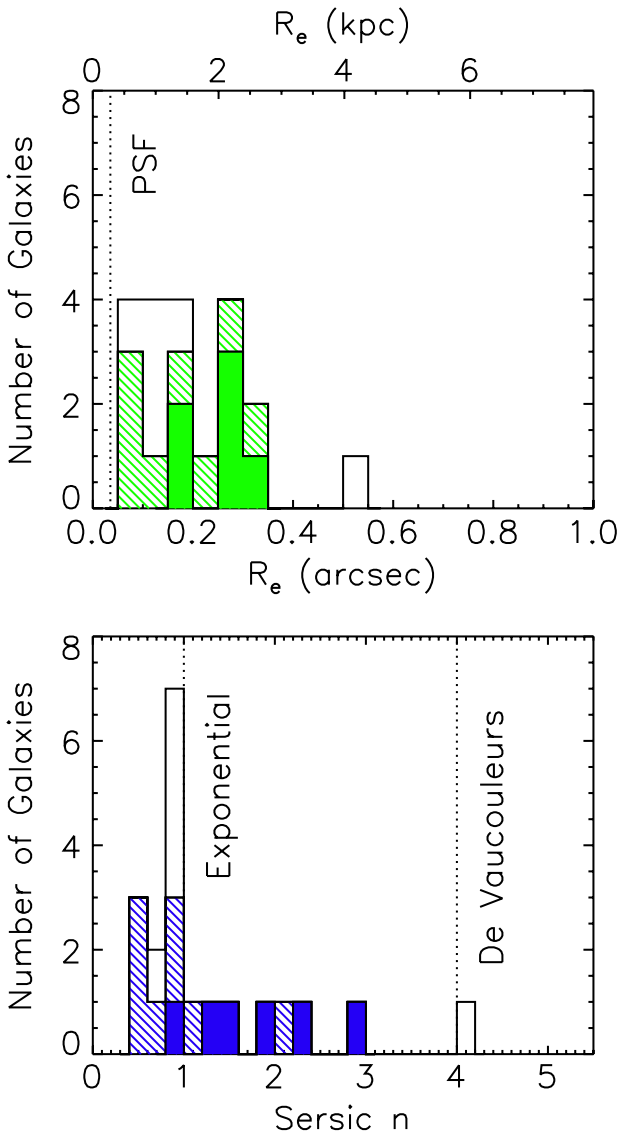

Figure 15. V_{606} morphologies derived using GALFIT for galaxies near LABd05. Open histograms contain all sources; solid and hatched histograms represent sources in groups "M1" and "M2," respectively (Section 3.1.3). Top: the histogram of galaxy effective radii (R_e), with the effective radius of the ACS PSF shown for reference (dotted line). Bottom: the histogram of Sérsic indices (n), with the values for exponential ($n = 1$) and De Vaucouleurs ($n = 4$) profiles shown for reference (dotted lines).

(A color version of this figure is available in the online journal.)

indices clustering around $n \approx 1$, indicative of exponential disk morphologies.

In summary, our analysis suggests that the LABd05 system hosts a large population of young, small, disky, low-luminosity galaxies.

4.2.3. Energy Budget of the Member Galaxies

The presence of a large population of compact galaxies within the LABd05 system raises an obvious question: are they responsible for powering the Lyα emission via photoionization? We find that the total ionizing luminosity ($L_{200-912\,\text{Å}}$) of all 16 of the well-detected nearby galaxies at the system redshift (excluding the obscured AGN, 36) is 8.5×10^{53}–6.6×10^{51} photons s^{-1} (unreddened, 5–25 Myr single bursts; Bruzual & Charlot 2003), ignoring the effects of distance, geometric corrections, and non-unity escape fractions. This is much less than is required to power the observed Lyα (1.7×10^{55} photons s^{-1}; Paper I). The fact that all of these galaxies lie tens of kiloparsecs away from the peak of the Lyα emission makes their potential contribution even smaller.

The only single compact source that could potentially contribute substantially to powering the nebula is the AGN (36), but simple energetic arguments imply that even it may not be powerful enough to explain all of the Lyα emission. In Paper I, we found that the total ionizing luminosity of the AGN, estimated from an extrapolation of the mid-infrared SED, was $\approx 1.8 \times 10^{54}$ photons s^{-1} and potentially orders of magnitude larger than the contribution from the other compact sources. There is a large associated uncertainty on this estimate due to the difficulty of extrapolating the ionizing luminosity from the mid-infrared SED, but if it is accurate, then it implies that the AGN can contribute at most 18% of the necessary ionizing photons to explain the Lyα (Paper I). Recently, Colbert et al. (2011) argued, based on measurements of polycyclic aromatic hydrocarbon (PAH) features in IRS spectroscopy, that roughly half of the bolometric luminosity of this mid-infrared source may arise from star formation rather than AGN activity. If so, then our estimate of the fraction of ionizing photons contributed by the AGN must be reduced by an additional factor of two. Thus, for the AGN to be the dominant power source for the Lyα nebula, the geometry of the system must be such that the AGN is highly obscured to our line of sight but relatively unobscured in the direction of the gas cloud. A full analysis of the energetics of the system and the dominant power source will be addressed in an upcoming paper.

4.3. An Offset Morphology with No Central Galaxy

A key observational result of this work is that there is no galaxy or AGN at or near the center of the Lyα nebula itself. All the compact sources visible in the *HST* imaging are offset by $\approx$20 kpc from the peak of the Lyα emission. In fact, the member galaxies actually appear to encircle the nebula (e.g., 1, 18, 21, 26, 29, 45, 52, 57), although given the small sample size, it is not clear whether or not this effect is significant or merely coincidental. Neither the Lyα nor the diffuse UV continuum components show any significant knots of emission that might represent bright star-forming galaxies or luminous stellar clusters. The lack of compact components brighter than 3.5×10^{-17} erg s^{-1} cm^{-2} (5σ) in the diffuse V_{606}-band light implies that there are no compact sources with luminosities brighter than $\sim 2 \times 10^{42}$ erg s^{-1} ($0.03\,L^*$) embedded within the central line-emitting region of the nebula. Similarly, the lack of any obvious substructure in the ACS Lyα image suggests that there are no compact sources forming stars at a rate greater than $\sim 1\ M_\odot$ yr^{-1}. The absence of 24 μm emission spatially associated with the Lyα nebula suggests there is also no hidden starburst at the center. This lack of a central galaxy has important implications for the potential power source in LABd05.

An early model that was proposed to explain the Lyα nebula phenomenon was shock-heating in starburst superwinds. However, from previous work we know that the C IV and He II line ratios in LABd05 are not consistent with shock ionization (Paper I). More importantly, with no central source present to drive a wind, it is extremely difficult to describe this system using a simple outflow model. An outflow driven by one of the other sources would need to be severely asymmetric (no secondary Lyα peak is present on the opposite side) and extend more than $\sim$40 kpc in one direction.

The lack of a central galaxy is similarly problematic for models that attempt to explain large Lyα nebulae such as LABd05 as evidence for cold flows. In this scenario, the Lyα is powered primarily via gravitational cooling radiation, as gas falls into a gravitational potential well along cold filaments, heats collisionally, and cools via Lyα. The theoretical expectation, borne out more recently in numerical simulations, is that the extended Lyα emission surrounds a growing galaxy (Haiman et al. 2000; Fardal et al. 2001; Furlanetto et al. 2005; Yang et al. 2006; Dijkstra et al. 2006a, 2006b; Goerdt et al. 2010; Faucher-Giguère et al. 2010). This basic prediction of the cold flow model is violated in the case of LABd05. In order to reconcile the data with this scenario, we would have to conclude that we are witnessing the Lyα nebula at an epoch *before* the star clusters within it have dynamically relaxed to form a centrally concentrated galaxy. Even in this case, since the observed centroid of the Lyα emission in this model should be a direct indication of the position of the center of mass of the system, we would need to understand how *all* of the compact sources—the luminous, obscured AGN and the 16 other compact galaxies—ended up $\gtrsim$20 kpc away from the center of mass.

Finally, another hypothesis for explaining the observed properties of Lyα nebulae is one in which Lyα photons produced by a central source are resonantly scattered in the surrounding gas out to much larger radii. Recent observations have uncovered what appear to be Lyα scattering halos around continuum-selected LBGs, with Lyα surface brightness profiles similar in shape to those of Lyα nebulae (Steidel et al. 2011), and have revived the long-standing question of whether Lyα nebulae could simply be scaled up versions of this phenomenon. In addition, imaging polarimetry of one of the $z = 3.1$ Lyα nebulae in the SSA22 field (LAB1) resulted in a detection of polarization of the Lyα emission (Hayes et al. 2011), suggesting that in this case Lyα photons may be scattering from central sources embedded within the nebula (see Weijmans et al. 2010) rather than being produced in situ at large radii. While resonant scattering must contribute at some level to the overall extent of Lyα nebulae, it is not yet clear whether this process is the dominant cause of the large sizes observed in all (or even most) Lyα nebulae. Indeed, this explanation is difficult to reconcile with our observations of LABd05. While existing imaging polarimetric constraints for LABd05 (Prescott et al. 2011) are not sufficient to rule out scattering entirely, with no central galaxy or galaxies, there is no obvious source of Lyα photons that could undergo resonant scattering to produce the observed Lyα nebula. Instead, the Lyα photons could only be supplied by the AGN or compact galaxies at the outskirts. The fact that the Lyα is so dramatically offset from these potential source(s) of Lyα photons would require that either the gas distribution or the illumination is severely asymmetric.

We note that LABd05 is not the only Lyα nebulae known to lack a central source. The extensive multi-wavelength imaging of the GOODS-S field revealed a Lyα-emitting nebula at $z \approx 3.16$ with no obvious continuum counterparts. This fact was used by the authors to argue that the Lyα emission is most likely powered by gravitational cooling radiation (Nilsson et al. 2006), which, if true, would again require the system to be in a very early state prior to the onset of significant star formation at or near the center of mass of the system. However, the deep *HST* multiband imaging of the field does reveal a number of compact galaxies within 1″–7″ of the Lyα emission peak. While none of the available photometric redshifts for these galaxies closely matches the redshift of the Lyα nebula, four of the brighter cases are consistent with the systemic redshift, given the large redshift error bars, and a number of fainter galaxies without reliable photometric redshifts are located within 1″–3″ of the Lyα emission peak. In the context of what we have learned about LABd05, it is clear that powerful Lyα nebulae can exist substantially offset from all associated continuum sources. We argue therefore that it remains to be seen whether the Nilsson et al. (2006) Lyα nebula is in fact alone.

4.4. Diffuse Line and Continuum Emission

The ACS and ground-based broadband images show clear evidence for a spatially extended diffuse UV continuum component that is co-located with the spatially extended Lyα emission. In addition, the non-detection in our narrowband *FR601N* imaging strongly suggests that the He II emission is spatially extended as well (0.″58 < FWHM < 1.″0). What is the origin of these diffuse components? Given the lack of a central galaxy, there are only two plausible sources: in situ spatially distributed star formation and/or the obscured AGN that lies >20 kpc away.

One intriguing possibility is that the diffuse UV continuum emission is due to star formation taking place in very small, widely distributed, perhaps dynamically unrelaxed regions that are unresolved and unseen by the current *HST* imaging. Possible evidence for this type of extended star formation has been seen in another radio-quiet Lyα nebula (SSA22-LAB1; Matsuda et al. 2007) as well as in the outskirts of a radio galaxy (MRC 1138-262, "the Spiderweb galaxy"; Hatch et al. 2008). This scenario would explain the morphology of the observed diffuse continuum component and the presence of ionizing radiation emerging over an extended region. The roughly elliptical shape of the UV continuum and Lyα components and the velocity profile of the Lyα reported in Paper I lead us to speculate that we could be observing a large, inclined disk exhibiting solid-body rotation. Using the central aperture measurements for both components (Table 4), we derive similar star formation rates from the Lyα and diffuse UV continuum emission (8.3 ± 0.1 and 5.6 ± 0.5 $M_\odot$ yr^{-1}, respectively, within the central 2 arcsec^2; Kennicutt 1998). The corresponding rest-frame equivalent width for Lyα is $\approx$200 $\pm$ 18 Å, which is plausible for a stellar population (Charlot & Fall 1993; Malhotra & Rhoads 2002; Schaerer 2003). However, the total diffuse UV continuum flux implies that the expected contribution to the ionizing photon flux is 1.7×10^{53}–1.3×10^{51} photons s^{-1} from a young (5–25 Myr), solar metallicity, spatially distributed stellar population with a mass of 5.0×10^7–4.6×10^8 $M_\odot$ (unreddened single bursts; Bruzual & Charlot 2003). This is only a fraction of the ionizing flux required to power the entire Lyα nebula (1.6×10^{55} photons s^{-1}; Paper I), suggesting that a much lower metallicity stellar population would be required in this scenario. The inferred spatial extent of the He II emission could potentially support this picture; however, this would imply a stellar population of extremely young age and low metallicity (<2 Myr, $Z < 10^{-7}$ $Z_\odot$; Schaerer 2003).

The alternative is that the diffuse line and continuum emission are the result of photoionization and scattering from the AGN located nearly 20 kpc away from the peak of the diffuse line and continuum components. Evaluating this scenario requires knowledge of the total power of the AGN and the degree of obscuration in the direction of the nebula. The bolometric luminosity derived from the infrared SED indicates a powerful AGN (8.6×10^{12} $L_\odot$; Yang et al. 2012). On the other hand, Colbert et al. (2011) found evidence for strong PAH emission

in the mid-infrared spectrum of this source and concluded that a significant fraction of the bolometric luminosity likely results from star formation as well. Hence, while an AGN beamed in the direction of the nebula but obscured from our direct view can account for some of the observed diffuse light, it is not yet clear what fraction of the observed Lyα and UV continuum emission can be explained by this scenario.

Ultimately, understanding the origin of the diffuse continuum components will require better data than are currently available. In particular, deep imaging to measure the continuum colors, deep polarization observations to determine what fraction, if any, of the continuum light is scattered, and a map of the velocity field measured from a non-resonant line (e.g., Hα or [O III]λ5007) are necessary. Given the apparent faintness and redshift of this target, these observations await the *James Webb Space Telescope*.

4.5. Smooth, Non-filamentary Morphology

Another key morphological result of this work is the finding that the diffuse emission components (Lyα and UV) in LABd05 are remarkably smooth and round. In particular, there is no evidence for the kind of bubble-like structures that have been taken as evidence for the superwind outflow scenario (e.g., Taniguchi et al. 2001; Mori et al. 2004; Matsuda et al. 2004). The diffuse emission is also not particularly clumpy or filamentary, in contrast to the predictions of recent cold flow simulations that suggest that the morphologies of Lyα nebulae powered by cold accretion should be asymmetric and narrow with "finger-like extensions" (Goerdt et al. 2010). Instead, the Lyα morphology of LABd05 is quite symmetric and well described by an exponential disk. While the typical axis ratios of the predicted Lyα nebulae appear (Figures 7–9 of Goerdt et al. 2010) to be in the range $b/a \approx 0.25$–0.5, LABd05 is much less elongated with an axis ratio of 0.79. The Goerdt et al. (2010) models also suggest that clumps associated with the inflowing streams should provide an important contribution to the total luminosity. Quantitative estimates are not given in the paper, but from their Figures 7–9 we estimate that there should be three to four significant clumps (with surface brightnesses >0.1 times that of the central peak) within the virial radius ($\approx$70 kpc). No significant clumps are seen in the Lyα emission from LABd05.

The surface brightness profiles of Lyα emission from model nebulae are also typically more centrally concentrated than that observed for LABd05. In Figure 9, we overplot the predicted surface brightness profiles from recent cold flow simulations. The Goerdt et al. (2010) prediction of a $r^{-1.2}$ power law, which we have scaled to match the total observed Lyα flux for LABd05 inside a radius of 5″, is a poor fit to the shape of the observed surface brightness profile. The Faucher-Giguère et al. (2010) predictions shown are based on their two most realistic treatments for Lyα emission from gravitational cooling (their models 7 and 9, which include prescriptions for self-shielding). The lower bound of each region shown corresponds to the prediction for a fiducial $2.5 \times 10^{11}\ M_{\odot}$ halo mass model at $z = 3$; the upper bound of each region is the same profile scaled up to a halo mass of $10^{13}\ M_{\odot}$ based on the predicted $L_{\mathrm{Ly}\alpha}$–M_{halo} relation (Faucher-Giguère et al. 2010) and under the naive assumption that the profile shape is constant as a function of halo mass. Model 7 can, in principle, reach the peak Lyα surface brightness we observe in LABd05, assuming a sufficiently massive halo, but the profile shape is much more centrally concentrated than is observed. Model 9 is orders of magnitude too faint, even for the most massive halos.

We note that although the expected luminosity scaling is the most basic output from models of Lyα nebulae powered by cold accretion, this has turned out to be particularly difficult to predict robustly. Early models suggested that the Lyα emission from gravitational cooling should be similar to what is observed in Lyα nebulae (e.g., Yang et al. 2006; Goerdt et al. 2010). However, more recent work has argued that these Lyα nebula luminosity predictions may be orders of magnitude too high due to the effects of self-shielding and that cooling radiation alone is an unlikely explanation for the Lyα emission of the most luminous Lyα nebulae (Faucher-Giguère et al. 2010). The question of the predicted Lyα luminosity from cold accretion is still a matter of some debate, but interestingly our analysis has shown that even if the question of the luminosity scaling is ignored, key morphological discrepancies remain between existing cold flow models and what is seen in LABd05.

4.6. Similar UV and Lyα Surface Brightness Profiles

Due to the effects of resonant scattering, there is a generic expectation that high-redshift sources of Lyα emission should be surrounded by low surface brightness halos of resonantly scattered Lyα emission (e.g., Loeb & Rybicki 1999; Zheng et al. 2010). After a number of observational studies uncovered possible hints of this extended emission in samples of Lyα-emitting galaxies (e.g., Hayashino et al. 2004; Ono et al. 2010), Steidel et al. (2011) used a stacking analysis to demonstrate convincingly that extended Lyα halos appear to exist around all classes of star-forming galaxies. They noted the large extent of these Lyα halos relative to the much more compact UV cores and pointed out the similarities in surface brightness profile shape between the Lyα halos around stacked continuum-selected LBGs and stacked Lyα nebulae in the same field. They concluded that, if one could image deeply enough ($F_{\mathrm{Ly}\alpha} \approx 10^{-19}$ erg s^{-1} cm^{-2}), then all continuum-selected LBGs would be classified as extended Lyα nebulae. The obvious question then becomes: are giant Lyα nebulae simply scaled up versions of this phenomenon with the large extent driven simply by resonant scattering of Lyα photons from a single or several central sources?

In the case of LABd05, it does not appear that the large Lyα extent can be explained simply as a result of resonant scattering. The lack of an obvious central source of Lyα photons is the first challenge (as discussed in Section 4.3), but another inconsistency appears when considering the Lyα and UV surface brightness profiles (Figure 10). Instead of a compact UV core surrounded by an extended Lyα halo, the UV emission in LABd05 is nearly as spatially extended as the Lyα, a clear indication that the nebula's large size is primarily the result of some other mechanism or geometry. Furthermore, the observed Lyα and diffuse UV continuum surface brightness profiles are remarkably similar in their properties. They both show similar radial distributions, are well described by nearly exponential disks, and have approximately elliptical shapes with similar axial ratios (Table 4). In comparison, the stacked UV and Lyα profiles derived for continuum-selected star-forming galaxies differ significantly (Figure 10; Steidel et al. 2011). Thus, while it seems likely that resonant scattering can explain some of the remaining differences between the two components, it does not appear that the large spatial extent of LABd05 is solely a result of Lyα resonant scattering.

4.7. A Galaxy Group in Formation?

LABd05 is unique only because of the existence of deep and high spatial resolution broad- and narrowband imaging data. These data provide many pieces of evidence in support of the idea that this is a young, forming system. There are numerous small, low-luminosity, disky galaxies, many of which have very blue colors. Even the reddest objects have colors that are consistent with ages of less than a few hundred million years, perhaps only a hundred million years if they are modestly reddened (i.e., $E(B-V) \approx 0.4$ mag). The large and luminous Lyα halo and the detection of faint, diffuse UV continuum emission in the region also suggest that the system is energetically young. In addition, the fact that nine of the compact galaxies that are likely to be associated with the system (i.e., roughly half the candidate members, with a total luminosity of 1.2 L^*) lie within a small projected area $\approx$30 kpc in diameter, suggests that the system may also be *dynamically young*, the dynamical time for this region being only $\sim$14 Myr.[19]

We speculate that this giant Lyα nebula is the progenitor of a galaxy group, witnessed in the process of formation. Under this assumption, the luminosity distribution of the member galaxies can provide a unique perspective on the "initial luminosity function" of galaxies. Spectroscopic redshift measurements of the galaxies within the system will be key to confirming membership and determining the total dynamical mass. While we only have spectroscopic redshifts for three sources in the region, we have argued both from the excess of galaxies in the vicinity of the nebula and from the colors of these galaxies that most of the compact objects observed are likely members of the system. By assuming that all the galaxies that lie above the dashed line in Figure 4 are members, we have constructed a luminosity function for LABDd05, as shown in Figure 14 (bottom panel). Summing all the UV luminosity contributed by the candidate member galaxies and the diffuse continuum results in a total of $\approx$23.4 AB mag in the V_{606} band, or $\approx 3\,L^*$. It is therefore possible that this system could evolve into a small group, with the smaller galaxies merging into larger systems over a few dynamical times.

Clearly, better data are needed, both to confirm the membership and to measure the stellar masses of the member galaxies more robustly. Nevertheless, LABd05 provides the tantalizing hope that detailed studies of more such systems, even statistical studies, can result in a determination of the initial mass function of galaxies, analogous to the manner in which studies of stellar clusters in our own Galaxy have yielded the stellar initial mass function. While LABd05 is only one source, we note that there are other Lyα nebulae that appear to be similar in morphology. For example, one of the Lyα nebulae in the SSA22 field at $z \approx 3.1$ (LAB1) shows multiple embedded galaxies and a hint of diffuse UV continuum in between the galaxies in ground-based data (Matsuda et al. 2007). As discussed in Section 4.3, the Lyα nebula found in the GOODS-S field at $z \approx 3.16$ has no central continuum counterpart (Nilsson et al. 2006). Deep *HST* imaging of a larger sample of giant Lyα nebulae will be important for understanding the extent to which the morphology and galaxy properties observed in LABd05 are characteristic of Lyα nebula systems in general.

[19] This calculation assumes that L^* corresponds to a mass of $\approx 2 \times 10^{10}\ M_\odot$ (Shapley et al. 2005; Reddy et al. 2006; Erb et al. 2006; Reddy & Steidel 2009) and a stellar-to-halo mass ratio at this mass of 10^{-2} for $z = 3$ (Moster et al. 2010).

5. CONCLUSIONS

Using high-resolution *HST* imaging, we have taken a census of all the compact sources within a large Lyα nebula at $z \approx 2.656$. We find that the Lyα nebula system contains numerous compact, young, disky galaxies and an obscured AGN that are all located tens of kiloparsecs from the peak of the Lyα emission and provide a negligible contribution to the ionization of the nebula. The observed luminosity function shows that the compact sources within the system are predominantly low luminosity ($\sim 0.1\,L^*$) galaxies, highly suggestive of a galaxy-forming environment. The large-scale morphology of the system is characterized by the lack of a central galaxy at or near the peak of the Lyα nebula and the presence of several nearly coincident, smooth, and spatially extended emission components (Lyα, He II, and diffuse UV continuum). These morphological results—in particular the lack of a central galaxy and the offset morphology—disfavor models of outflows, cold flows, and resonant scattering halos, suggesting that while these phenomena may be present, they are not sufficient to explain the powering and the large extent of giant Lyα nebulae. Based on these observations, we speculate that large Lyα nebulae are progenitors of low-redshift galaxy groups or low-mass clusters.

The authors thank Kate Brand, Galina Soutchkova, and Sangeeta Malhotra for their assistance with the *HST* observation planning and execution. We are grateful to Crystal Martin, Kristian Finlator, Avi Loeb, Dan Weedman, Tommaso Treu, Matt Auger, and the anonymous referee for useful discussions and suggestions. M.K.M.P. acknowledges support from an NSF Graduate Research Fellowship, a P.E.O. Fellowship, and a TABASGO Prize Postdoctoral Fellowship. This work was based on observations made with the NASA/ESA *Hubble Space Telescope* (*HST* Cycle 14; GO#10591), obtained at the Space Telescope Science Institute, which is operated by the Association of Universities for Research in Astronomy, Inc., under NASA contract NAS 5-26555. This work is also based in part on data collected at the Subaru Telescope, which is operated by the National Astronomical Observatory of Japan, and on data from the NOAO Deep Wide-Field Survey (B. Jannuzi, A. Dey) as distributed by the NOAO Science Archive. A.D. and B.T.J.'s research activities are supported by NOAO. NOAO is operated by the Association of Universities for Research in Astronomy (AURA), Inc. under a cooperative agreement with the National Science Foundation. V.D. and B.T.S. are supported by the *Spitzer Space Telescope* project, which is managed by JPL on behalf of NASA.

Facilities: HST, Subaru, Mayall

APPENDIX

POSTAGE STAMPS

Postage stamp images of the compact sources in the vicinity of LABd05 are shown in Figure 16. From left to right, the panels display the stacked image and the individual V_{606}-, J_{110}-, and H_{160}-band images. Object ID numbers are shown in the upper left-hand corner of the stacked image, and the membership category (where applicable) is given in the upper right-hand corner. The AGN (36) and both components of the LBG (26 and 59) are labeled in the lower right-hand corner.

We note that the current data are not sufficient to distinguish whether the object pairs (26+59, 1+57, 21+58, and 46+60) are

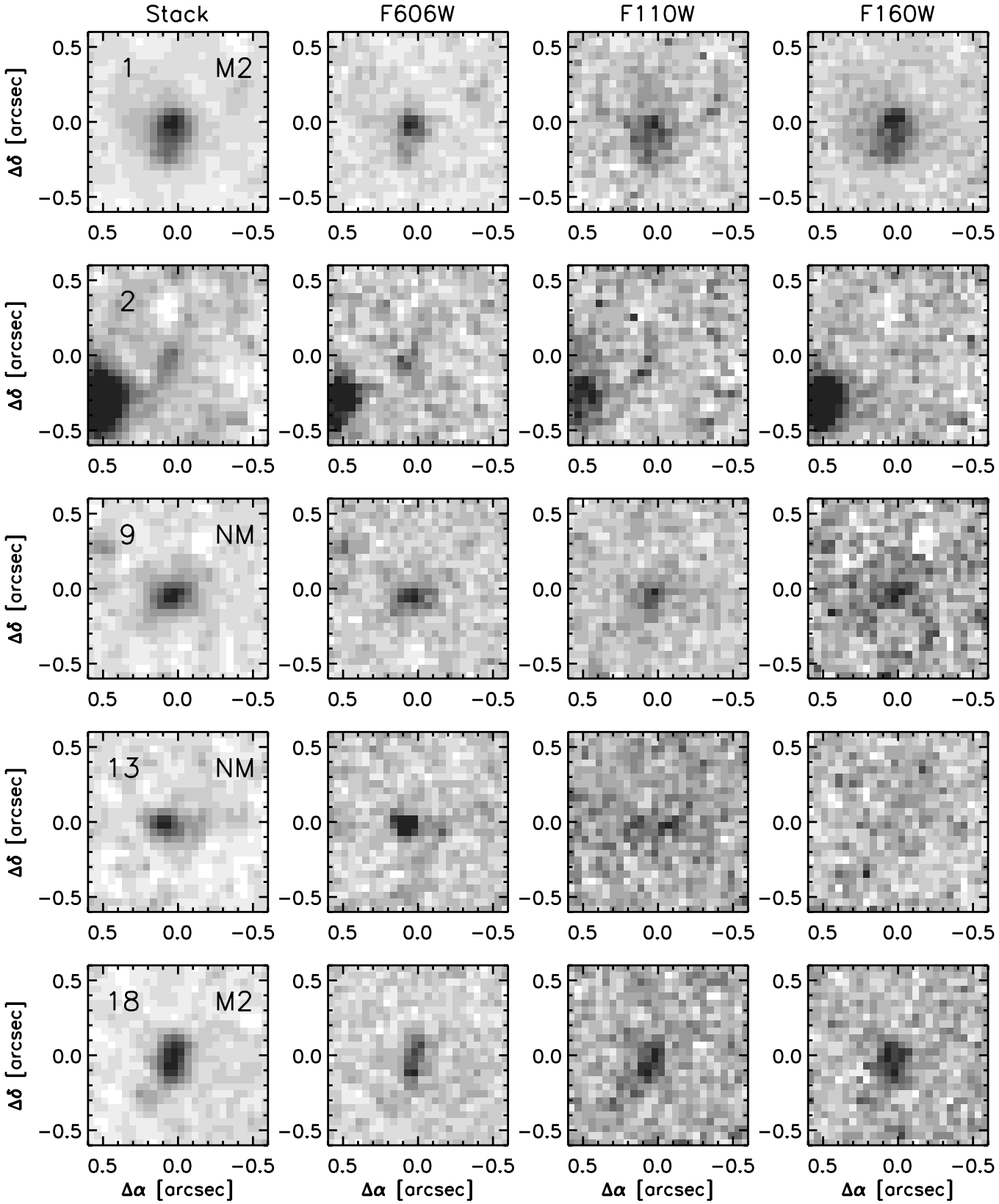

Figure 16. Postage stamp images of the compact sources in the vicinity of LABd05.

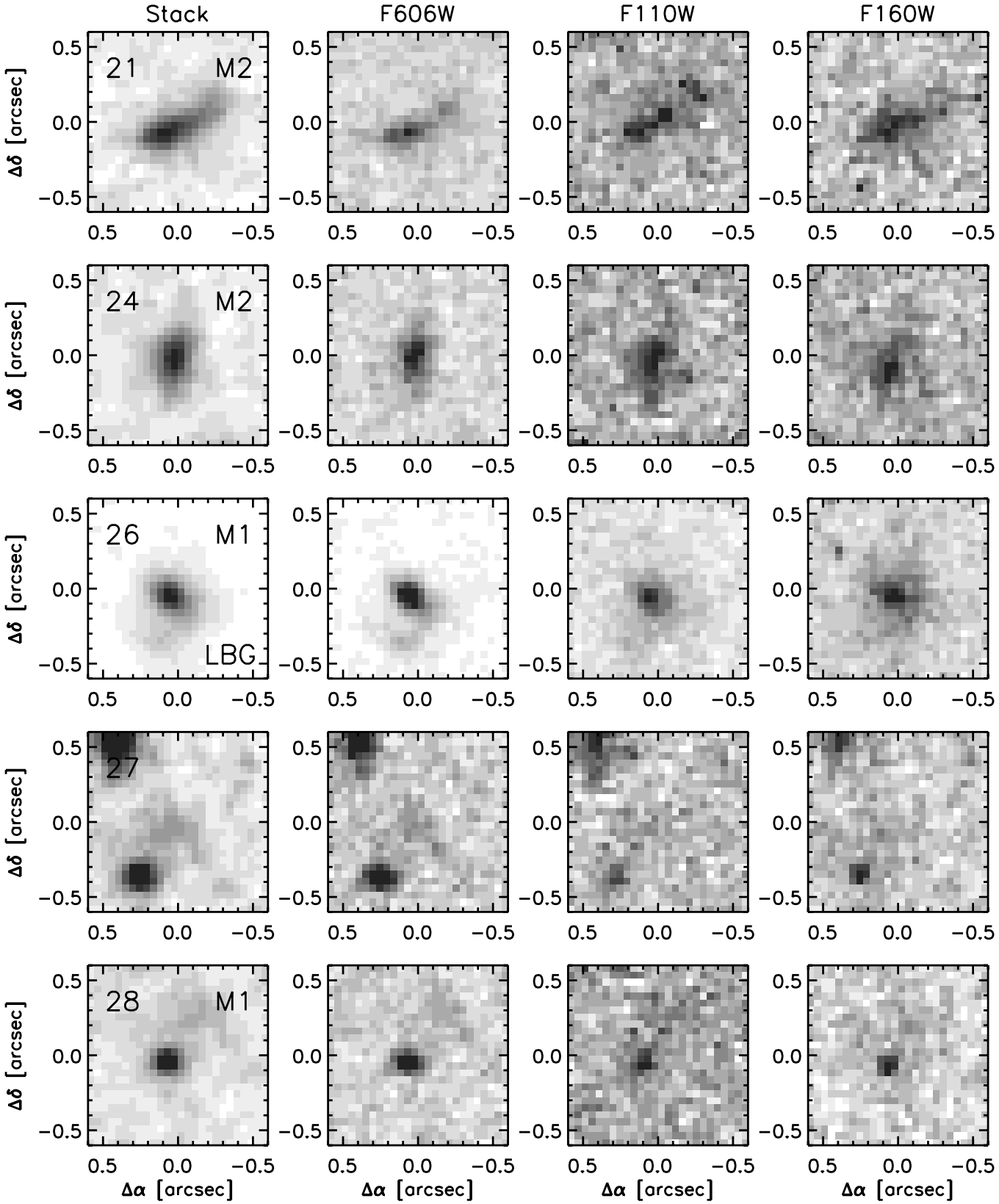

Figure 16. (Continued)

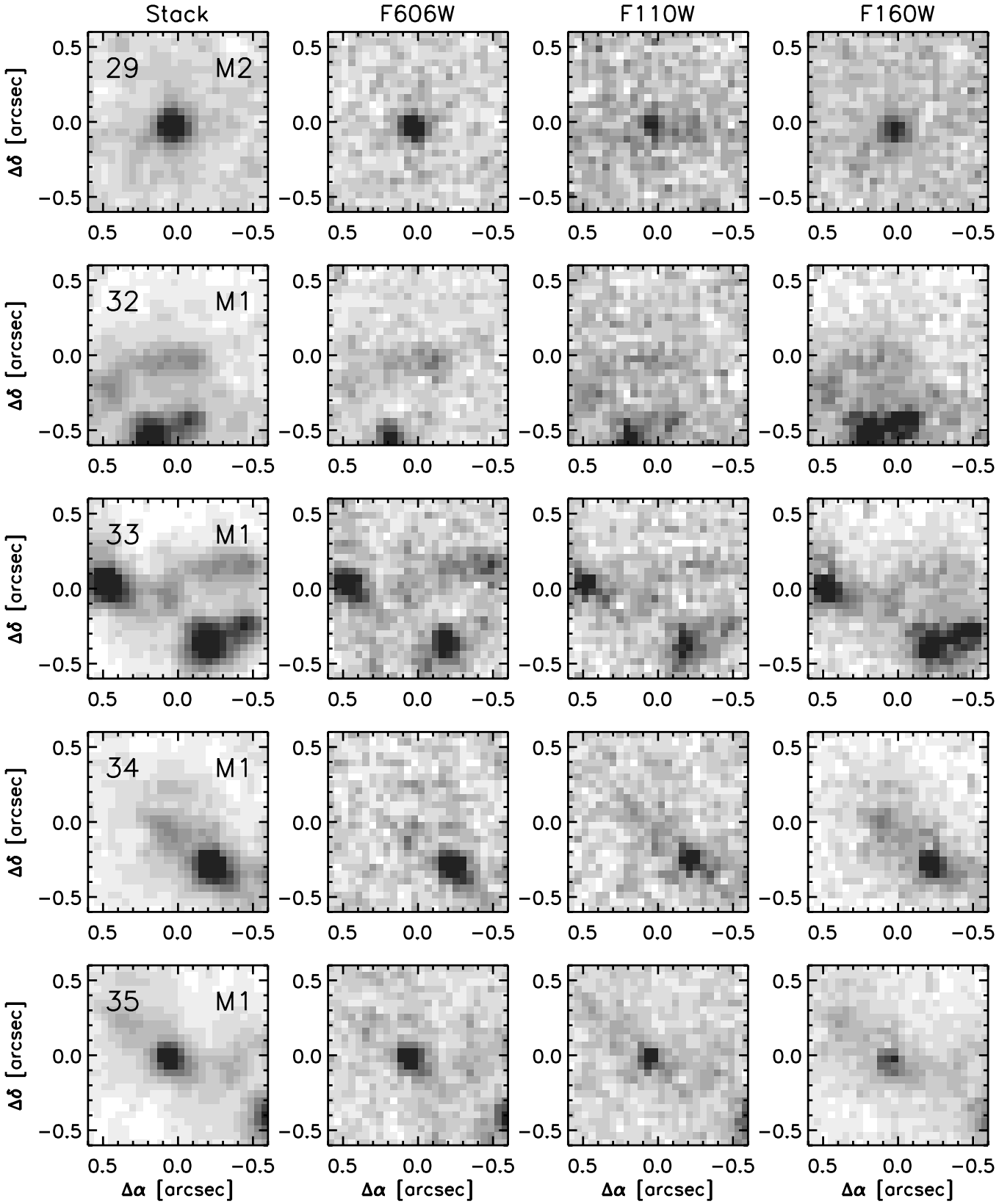

Figure 16. (Continued)

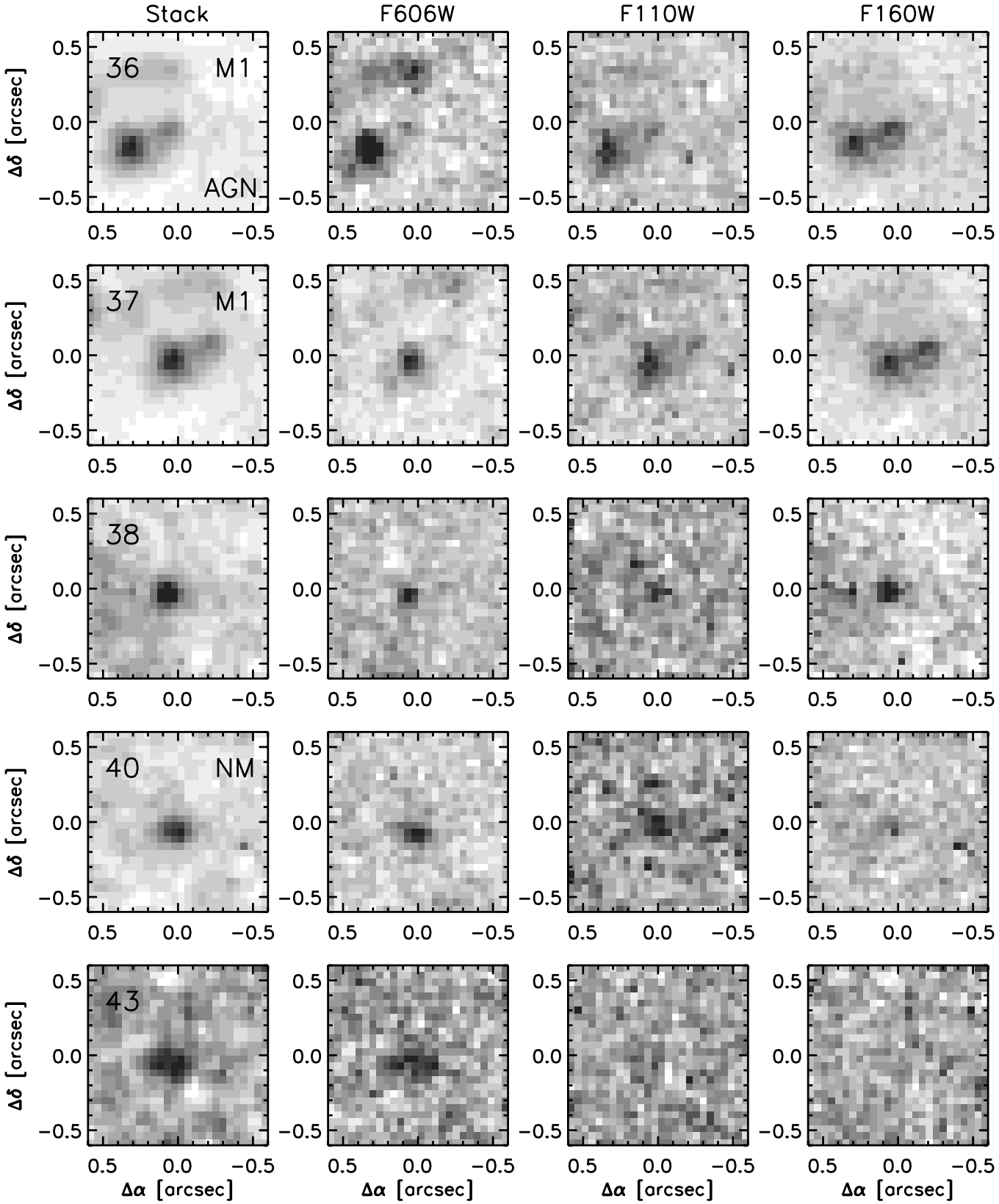

Figure 16. (Continued)

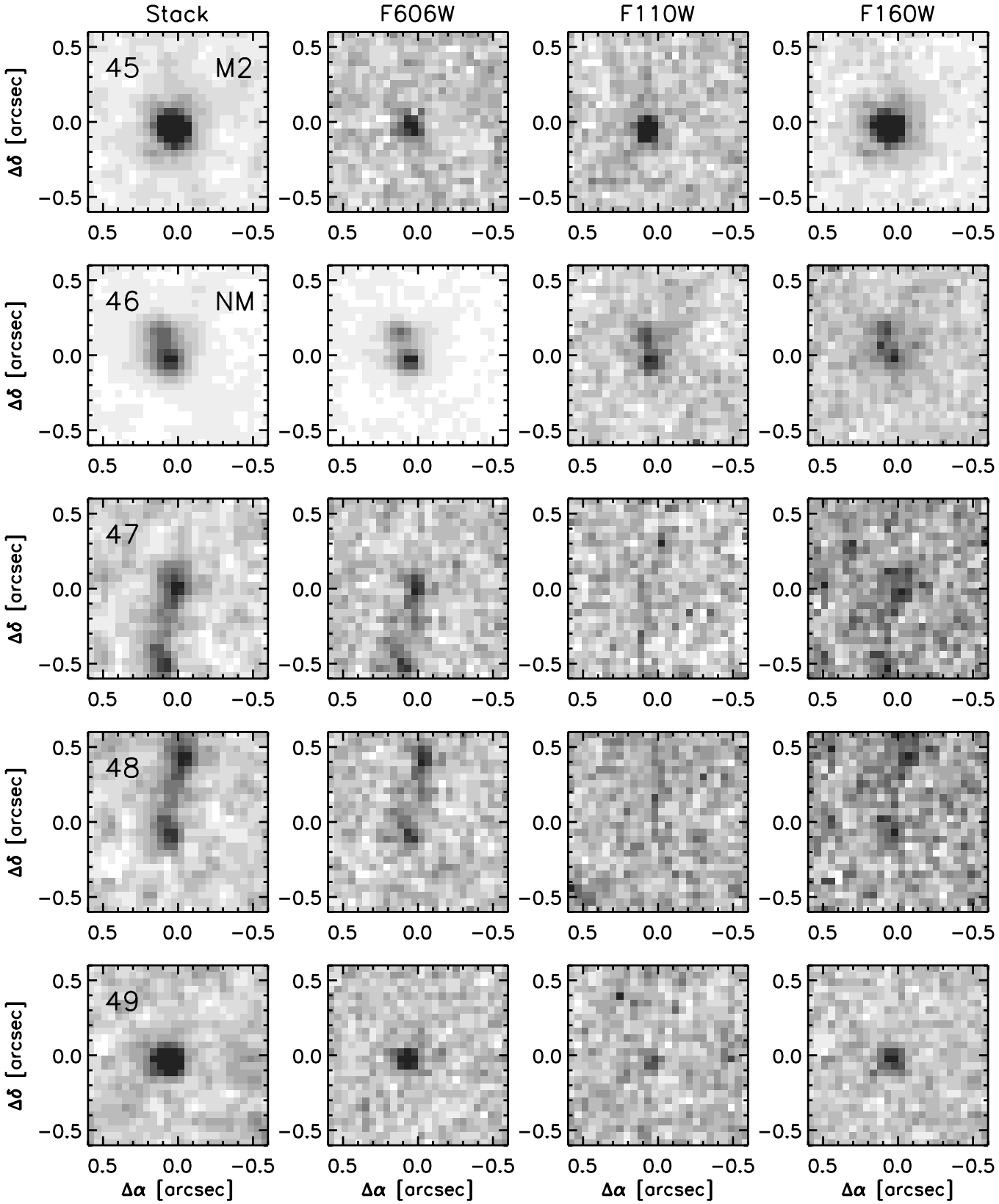

Figure 16. (Continued)

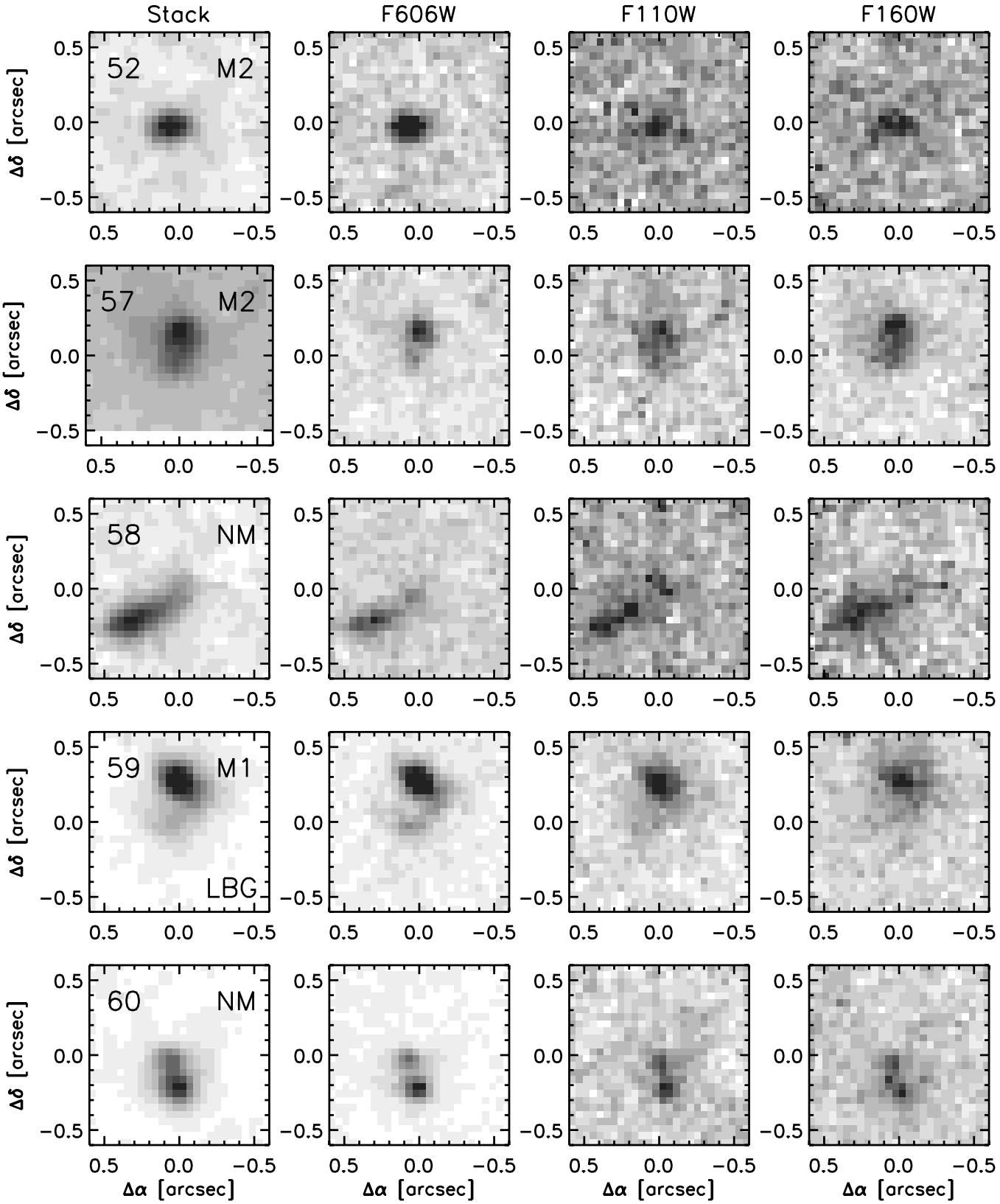

Figure 16. (Continued)

true companions or just morphological peculiarities (i.e., tidal features, dust lanes, etc.) associated with the primary object. For our analysis, we have chosen to treat each of the object pairs as two separate objects. Treating them each as a single object would decrease the number of sources in the "M1" category by one and the "M2" category by two, but this does not significantly alter our conclusions regarding the nature of the member galaxies or the overall luminosity function within the LABd05 system.

REFERENCES

Alonso-Herrero, A., Pérez-González, P. G., Alexander, D. M., et al. 2006, ApJ, 640, 167
Barrio, F. E., Jarvis, M. J., Rawlings, S., et al. 2008, MNRAS, 389, 792
Basu-Zych, A., & Scharf, C. 2004, ApJ, 615, L85
Beckwith, S. V. W., Stiavelli, M., Koekemoer, A. M., et al. 2006, AJ, 132, 1729
Bertin, E., & Arnouts, S. 1996, A&AS, 117, 393
Bruzual, G., & Charlot, S. 2003, MNRAS, 344, 1000
Bussmann, R. S., Dey, A., Borys, C., et al. 2009, ApJ, 705, 184
Casertano, S., de Mello, D., Dickinson, M., et al. 2000, AJ, 120, 2747
Chapman, S. C., Scott, D., Windhorst, R. A., et al. 2004, ApJ, 606, 85
Charlot, S., & Fall, S. M. 1993, ApJ, 415, 580
Coe, D., Benítez, N., Sánchez, S. F., et al. 2006, AJ, 132, 926
Colbert, J. W., Scarlata, C., Teplitz, H., et al. 2011, ApJ, 728, 59
Dey, A., Bian, C., Soifer, B. T., et al. 2005, ApJ, 629, 654
Dijkstra, M., Haiman, Z., & Spaans, M. 2006a, ApJ, 649, 14
Dijkstra, M., Haiman, Z., & Spaans, M. 2006b, ApJ, 649, 37
Dijkstra, M., & Loeb, A. 2009, MNRAS, 400, 1109
Eisenhardt, P. R., Stern, D., Brodwin, M., et al. 2004, ApJS, 154, 48
Erb, D. K., Steidel, C. C., Shapley, A. E., et al. 2006, ApJ, 646, 107
Fardal, M. A., Katz, N., Gardner, J. P., et al. 2001, ApJ, 562, 605
Faucher-Giguère, C.-A., Kereš, D., Dijkstra, M., Hernquist, L., & Zaldarriaga, M. 2010, ApJ, 725, 633
Francis, P. J., Woodgate, B. E., Warren, S. J., et al. 1996, ApJ, 457, 490
Furlanetto, S. R., Schaye, J., Springel, V., & Hernquist, L. 2005, ApJ, 622, 7
Geach, J. E., Alexander, D. M., Lehmer, B. D., et al. 2009, ApJ, 700, 1
Geach, J. E., Smail, I., Chapman, S. C., et al. 2007, ApJ, 655, L9
Giavalisco, M., Ferguson, H. C., Koekemoer, A. M., et al. 2004, ApJ, 600, L93
Goerdt, T., Dekel, A., Sternberg, A., et al. 2010, MNRAS, 407, 613
Gorjian, V., Brodwin, M., Kochanek, C. S., et al. 2008, ApJ, 679, 1040
Haiman, Z., Spaans, M., & Quataert, E. 2000, ApJ, 537, L5
Hatch, N. A., Overzier, R. A., Röttgering, H. J. A., Kurk, J. D., & Miley, G. K. 2008, MNRAS, 383, 931
Hayashino, T., Matsuda, Y., Tamura, H., et al. 2004, AJ, 128, 2073
Hayes, M., Scarlata, C., & Siana, B. 2011, Nature, 476, 304
Houck, J. R., Soifer, B. T., Weedman, D., et al. 2005, ApJ, 622, L105
Ivison, R. J., Smail, I., Le Borgne, J.-F., et al. 1998, MNRAS, 298, 583
Jannuzi, B. T., & Dey, A. 1999, in ASP Conf. Ser. 191, Photometric Redshifts and the Detection of High Redshift Galaxies, ed. R. Weymann, L. Storrie-Lombardi, M. Sawicki, & R. Brunner (San Francisco, CA: ASP), 111
Jedrzejewski, R., Hack, W., Hanley, C., Busko, I., & Koekemoer, A. M. 2005, in ASP Conf. Ser. 347, Astronomical Data Analysis Software and Systems XIV, ed. P. Shopbell, M. Britton, & R. Ebert (San Francisco, CA: ASP), 129
Kennicutt, R. C. 1998, ARA&A, 36, 189
Loeb, A., & Rybicki, G. B. 1999, ApJ, 524, 527
Magee, D. K., Bouwens, R. J., & Illingworth, G. D. 2007, in ASP Conf. Ser. 376, Astronomical Data Analysis Software and Systems XVI, ed. R. A. Shaw, F. Hill, & D. J. Bell (San Francisco, CA: ASP), 261
Malhotra, S., & Rhoads, J. E. 2002, ApJ, 565, L71
Matsuda, Y., Iono, D., Ohta, K., et al. 2007, ApJ, 667, 667
Matsuda, Y., Nakamura, Y., Morimoto, N., et al. 2009, MNRAS, 400, L66
Matsuda, Y., Yamada, T., Hayashino, T., et al. 2004, AJ, 128, 569
Matsuda, Y., Yamada, T., Hayashino, T., et al. 2005, ApJ, 634, L125
Matsuda, Y., Yamada, T., Hayashino, T., et al. 2011, MNRAS, 410, L13
McCarthy, P. J. 1993, ARA&A, 31, 639
Miley, G. K., Overzier, R. A., Zirm, A. W., et al. 2006, ApJ, 650, L29
Miyazaki, S., Komiyama, Y., Sekiguchi, M., et al. 2002, PASJ, 54, 833
Mori, M., Umemura, M., & Ferrara, A. 2004, ApJ, 613, L97
Moster, B. P., Somerville, R. S., Maulbetsch, C., et al. 2010, ApJ, 710, 903
Nilsson, K. K., Fynbo, J. P. U., Møller, P., Sommer-Larsen, J., & Ledoux, C. 2006, A&A, 452, L23
Oke, J. B. 1974, ApJS, 27, 21
Ono, Y., Shimasaku, K., Dunlop, J., et al. 2010, ApJ, 724, 1524
Ouchi, M., Ono, Y., Egami, E., et al. 2009, ApJ, 696, 1164
Palunas, P., Teplitz, H. I., Francis, P. J., Williger, G. M., & Woodgate, B. E. 2004, ApJ, 602, 545
Peng, C. Y., Ho, L. C., Impey, C. D., & Rix, H.-W. 2002, AJ, 124, 266
Prescott, M. K. M. 2009, PhD thesis, Univ. Arizona
Prescott, M. K. M., Dey, A., & Jannuzi, B. T. 2009, ApJ, 702, 554
Prescott, M. K. M., Kashikawa, N., Dey, A., & Matsuda, Y. 2008, ApJ, 678, L77
Prescott, M. K. M., Smith, P. S., Schmidt, G. D., & Dey, A. 2011, ApJ, 730, L25
Reddy, N. A., & Steidel, C. C. 2009, ApJ, 692, 778
Reddy, N. A., Steidel, C. C., Erb, D. K., Shapley, A. E., & Pettini, M. 2006, ApJ, 653, 1004
Reddy, N. A., Steidel, C. C., Pettini, M., et al. 2008, ApJS, 175, 48
Saito, T., Shimasaku, K., Okamura, S., et al. 2006, ApJ, 648, 54
Schaerer, D. 2003, A&A, 397, 527
Shapley, A. E., Steidel, C. C., Erb, D. K., et al. 2005, ApJ, 626, 698
Smith, D. J. B., & Jarvis, M. J. 2007, MNRAS, 378, L49
Smith, D. J. B., Jarvis, M. J., Lacy, M., & Martínez-Sansigre, A. 2008, MNRAS, 389, 799
Smith, D. J. B., Jarvis, M. J., Simpson, C., & Martínez-Sansigre, A. 2009, MNRAS, 393, 309
Steidel, C. C., Adelberger, K. L., Shapley, A. E., et al. 2000, ApJ, 532, 170
Steidel, C. C., Bogosavljević, M., Shapley, A. E., et al. 2011, ApJ, 736, 160
Taniguchi, Y., & Shioya, Y. 2000, ApJ, 532, L13
Taniguchi, Y., Shioya, Y., & Kakazu, Y. 2001, ApJ, 562, L15
Weidinger, M., Møller, P., Fynbo, J. P. U., & Thomsen, B. 2005, A&A, 436, 825
Weijmans, A.-M., Bower, R. G., Geach, J. E., et al. 2010, MNRAS, 402, 2245
Williams, R. E., Blacker, B., Dickinson, M., et al. 1996, AJ, 112, 1335
Yang, Y., Decarli, R., Dannerbauer, H., et al. 2012, ApJ, 744, 178
Yang, Y., Zabludoff, A., Eisenstein, D., & Davé, R. 2010, ApJ, 719, 1654
Yang, Y., Zabludoff, A., Jahnke, K., et al. 2011, ApJ, 735, 87
Yang, Y., Zabludoff, A., Tremonti, C., Eisenstein, D., & Davé, R. 2009, ApJ, 693, 1579
Yang, Y., Zabludoff, A. I., Dave, R., et al. 2006, ApJ, 640, 539
Zheng, Z., Cen, R., Weinberg, D., Trac, H., & Miralda-Escude, J. 2010, ApJ, 739, 62